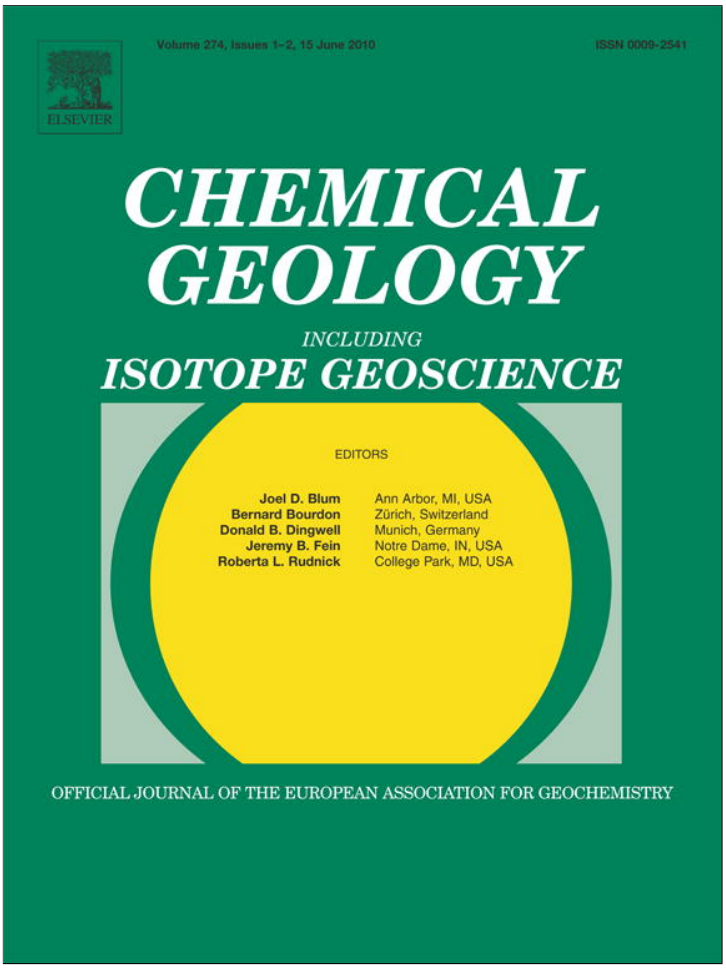

Chemical Geology 274 (2010) 68–81

Contents lists available at ScienceDirect

Chemical Geology

journal homepage: www.elsevier.com/locate/chemgeo

Research paper

Dissolution–reprecipitation of igneous zircon in mid-ocean ridge gabbro, Atlantis Bank, Southwest Indian Ridge

Joshua J. Schwartz [a,*], Barbara E. John [b], Michael J. Cheadle [b], Joseph L. Wooden [c], Frank Mazdab [c,1], Susan Swapp [b], Craig B. Grimes [d]

[a] Department of Geological Sciences, University of Alabama, Tuscaloosa, AL 35487, United States
[b] Department of Geology and Geophysics, University of Wyoming, Laramie, WY 82071, United States
[c] U.S.G.S.-Stanford Ion Probe Laboratory, Stanford, CA 94305, United States
[d] Department of Geosciences, Mississippi State University, Mississippi State, MS 39762, United States

ARTICLE INFO

Article history:
Received 20 November 2009
Received in revised form 25 March 2010
Accepted 28 March 2010

Editor: R.L. Rudnick

Keywords:
Dissolution–reprecipitation
U–Pb zircon geochronology
Zircon geochemistry
EBSD
Atlantis Bank
Mid-ocean ridge

ABSTRACT

Zircons recovered from oceanic gabbro exposed on Atlantis Bank, Southwest Indian Ridge, typically display oscillatory and sector zoning consistent with igneous crystallization from mafic magmas. In one rock (of twenty investigated), weak-oscillatory-zonation patterns are overprinted by secondary textural features characterized by mottled, convoluted and wavy internal zonation patterns that are frequently associated with secondary micron- to submicron-scale micro-porosity. These zircons are hosted in a felsic vein that intruded an oxide gabbro, both of which are cross-cut by monomineralic amphibole- and quartz-rich veinlets. Zircons with weak-oscillatory-zonation patterns record a weighted-average $^{206}Pb/^{238}U$ age of 12.76 ± 0.20 Ma (mswd = 1.5), and have high trace element concentrations [e.g., ΣREEs (~0.4–2.2 wt.%), Y (~0.6–2.8 wt.%), P (~0.4–0.9 wt.%)], and Th/U (0.1–0.5). These zircons are anomalously old (≥1 Myr) relative to the magnetic age for this portion of oceanic crust (11.75 Ma). In contrast, zircons with non-igneous, secondary textures have a younger weighted-average $^{206}Pb/^{238}U$ age of 12.00 ± 0.16 Ma (mswd = 1.7), and have lower trace element concentrations [e.g., ΣREEs (~0.2–0.8 wt.%), Y (~0.3–1.0 wt.%), P (~0.1–0.3 wt.%)], and slightly lower Th/U (0.1–0.3). The weighted-average age of these zircons is similar to the magnetic anomaly age, and other $^{206}Pb/^{238}U$ ages of nearby rocks. We do not observe a correlation between crystallographic misorientation, internal texture, or trace element chemistry. We suggest that the decrease in trace element concentrations associated with the development of non-igneous alteration textures is attributed to the purging of non-essential structural constituent cations from the zircon crystal lattice at amphibolite-facies conditions. The mechanism of alteration/re-equilibration was likely an interface-coupled dissolution–reprecipitation processes that affected pre-existing, anomalously old zircons during shallow-level magmatic construction of Atlantis Bank at ~12.0 Ma.

1. Introduction

Zircon is a relatively common trace mineral in oceanic crust and has been reported from both slow-spreading and fast-spreading mid-ocean ridges (e.g., Cannat et al., 1995; Gillis, 1996; John et al., 2004; Schwartz et al., 2005; Coogan and Hinton, 2006; Grimes et al., 2007; Baines et al., 2009; Grimes et al., 2009; Lissenberg et al., 2009). Zircons from mid-ocean ridge crust typically display weak-oscillatory-zonation (WOZ) patterns characteristic of zircons crystallized from mafic magmas (Tomaschek et al., 2003; McLelland et al., 2004; Grimes et al., 2007; Baines et al., 2009; Grimes et al., 2009). Here, we discuss a class of zircons that are distinguished by mottled and chaotic internal textures indicating chemical modification and/or re-equilibration after igneous crystallization. Zircons with similar textures have previously been reported from complexly deformed and metamorphosed ophiolites and continental terranes (Tomaschek et al., 2003; Spandler et al., 2004; Puga et al., 2005). The fact that these zircons are found in *in-situ* oceanic crust allows us to investigate the processes that lead to modification of zircon in mid-ocean ridge environments. These processes are important for understanding timescales of magmatism, hydrothermal alteration, and chemical fluxes at slow-spreading mid-ocean ridges.

The development of secondary, non-igneous alteration textures indicates that zircons were not in chemical equilibrium with their environment after original igneous crystallization and were subject to processes that may have resulted in changes in internal chemistry. These processes can include a variety of mechanisms such as coupled dissolution–reprecipitation (Tomaschek et al., 2003; Geisler et al., 2007), diffusion–reaction–re-equilibration facilitated by the presence of

* Corresponding author. Tel.: +1 205 348 1878; fax: +1 205 348 0818.
E-mail address: jschwartz@geo.ua.edu (J.J. Schwartz).
[1] Present address: Dept. of Geosciences, University of Arizona, Tucson, AZ 85721, United States.

0009-2541/$ – see front matter © 2010 Elsevier B.V. All rights reserved.
doi:10.1016/j.chemgeo.2010.03.017

an aqueous fluid (Geisler et al., 2003a,b, 2007), static grain-boundary and defect migration (e.g., Hoskin and Black, 2000), and deformation-enhanced diffusion along high diffusivity pathways (e.g., Timms et al., 2006; Reddy et al., 2006, 2007, 2009). The driving force(s) for re-equilibration can be either the reduction of lattice strain resulting from high concentrations of trace element 'impurities' in solid solution (Hoskin and Black, 2000; Tomaschek et al., 2003), or in metamict zircons, recovery of structural damage caused by self-irradiation (Chakoumakos et al., 1987; Murakami et al., 1991; Geisler et al., 2003a). Understanding these processes and their effects on zircon crystal chemistry is crucial for the correct interpretation of zircon geochronologic and geochemical data and for understanding the significance of those data in the context of the tectonic, magmatic and metamorphic history of the sample.

The purpose of this paper is to describe in detail the internal structures of altered/re-equilibrated zircons from one sample of oceanic gabbro collected from Atlantis Bank, Southwest Indian Ocean. In this study, we link textural observations with Pb/U ages, trace element geochemical data and representative electron backscattered diffraction maps from twenty-one igneous zircons, which have undergone varying degrees of secondary alteration/re-equilibration. Our data allow us to examine both magmatic and alteration processes, including 1) the timing of igneous crystallization and subsequent alteration/re-equilibration, 2) the behavior of trace- and rare earth elements during alteration/re-equilibration, and 3) mechanisms for chemical mobility (e.g., coupled dissolution–reprecipitation, dynamic and static re-equilibration) during alteration/re-equilibration on the seafloor. We suggest that decreasing trace element and REE concentrations reflect the expulsion of non-essential structural cations (e.g., P, REEs, Y, and Pb) from originally igneous domains. The patterns we observe cannot be explained by simple volume diffusion mechanisms, metamictization of the zircon lattice, nor deformation-enhanced chemical mobility. We suggest that coupled dissolution–reprecipitation of these zircons may explain many of the chemical and textural variations we observe.

2. Geology of Atlantis Bank

The Southwest Indian Ridge (SWIR) is a transitional slow- to ultraslow-spreading mid-ocean ridge (Dick et al., 1991b, 2003) that separates the Antarctic and Indian plates (Fig. 1 inset). Atlantis Bank lies approximately 100-km south of the SWIR rift valley where the long-term seafloor spreading half rate is estimated at 8.5 mm/yr for the Antarctic plate (Dick et al., 1991b; Hosford et al., 2003; Baines et al., 2007). Recently, Baines et al. (2008) estimated a seafloor spreading rate of 14.1 mm/yr during the creation of Atlantis Bank. Based on drilling, dredging, manned submersible and ROV observations, Atlantis Bank consists of variably deformed and denuded lower oceanic crust and upper mantle (Cannat et al., 1991a; Dick et al., 1991a, 2000; Natland and Dick, 2002). Rocks from ODP Hole 735B and from submersible dives at Atlantis Bank include olivine gabbro, olivine gabbronorite, and oxide gabbro with minor felsic veins (Dick et al., 1991a, 2000; Robinson et al., 2000; Natland and Dick, 2001, 2002). Oxide gabbros and felsic veins compose ~25% of core recovered from ODP Hole 735B and commonly host trace minerals (e.g., apatite, zircon, and titanite) suitable for geochronologic and thermochrologic dating (John et al., 2004). Pb/U geochronologic ages from Atlantis Bank range from 10.80 to 14.00 Ma (John et al., 2004; Schwartz et al., 2005; Baines et al., 2009). Some ages are anomalously old and may reflect assimilation of pre-existing gabbroic rocks from the mantle lithosphere (Schwartz et al., 2005).

Structurally, Atlantis Bank forms the footwall of a long-lived detachment fault system. Detachment faulting is thought to have occurred during the final stages of magmatic accretion (Natland and Dick, 2002) and likely rooted in the rift valley. High-temperature (>650 °C) deformation fabrics including mylonites are common (Cannat et al., 1991a; Dick et al., 2000; Miranda, 2006), and are overprinted by extensively altered cataclasites, locally ultracataclasites, and rare gouge. Core samples from ODP Hole 735B exhibit magmatic and metamorphic fabrics ranging down-temperature from submagmatic, granulite (650°–900 °C), amphibolite (450°–650 °C), greenschist (300°–450 °C) and sub-greenschist grades (Cannat et al., 1991b; Dick et al., 2000; Miranda, 2006). Microstructural and mineral thermometry indicate that ductile deformation initiated at high temperatures (>900 °C) and continued to lower temperatures as fault rocks were denuded along the detachment fault system (Miranda, 2006). Semi-brittle greenschist-grade fabrics in gabbro mylonites preserve the subsequent lower-temperature history at temperatures of ~250° to 350 ° C (Miranda, 2006). Active slip on the detachment fault system ceased as the footwall emerged at the rift valley wall, and was denuded to the seafloor, approximately 500 kyr after formation (Baines et al., 2008).

3. Sample description and analytical methods

We analyzed twenty-one zircon grains from sample JR-31 29-2, collected by dredging during *RRS James Clark Ross* Leg 31 (MacLeod et al., 1998). The sample was collected along the western flank of Atlantis Bank, ~5 km SW of ODP Hole 725B (lat: 57.2018 to 57.2118; long: −32.7507 to −32.7507), between 2644 and 2895 m water depth (Fig. 1). Sample JR-31 29-2 is an oxide gabbro intruded by feldspar- and quartz-bearing felsic vein, in turn intruded by a quartz vein (Fig. 2). Mineralogy of the host oxide gabbro comprises plagioclase, clinopyroxene, ilmenite, green and brown hornblende, actinolite and apatite. Laths of plagioclase occur along the right-side of the thin section in Fig. 2 and are relatively undeformed. In many cases, large clinopyroxene grains are replaced by brown hornblende along grain boundaries. In some cases, clinopyroxene cores are retrogressed to mats of fine-grained actinolite surrounded by rims of dark green and brown hornblende. Large plagioclase laths are cut by anastomosing networks of albite veinlets that sometimes parallel brown and dark green hornblende veinlets. The fine- to medium-grained felsic vein cross-cuts the oxide gabbro and displays graphic and micrographic textures characterized by fine-grained intergrowths of feldspar and quartz. The felsic vein is composed of quartz, plagioclase (and possibly fine-grained alkali feldspar), clinopyroxene and titanite. Clinopyroxene in the felsic vein is anhedral, lacks exsolution textures and unlike clinopyroxenes in the oxide gabbro does not display evidence for multiple alteration events by retrogression of amphibole. The felsic vein is cut by fractures and hornblende veinlets, and is intruded by a late-stage syntaxial quartz-rich vein (Fig. 2). Zircon (visible in thin section and scanning electron microscope) occurs in the felsic vein.

Deformation in the oxide gabbro host rock is localized (center of the thin section: Fig. 2) and involved dislocation creep accompanied by dynamic re-equilibration of plagioclase and clinopyroxene. Both clinopyroxene and plagioclase grains have well-developed mantles of subgrains with porphyroclasts displaying kink-banding. The felsic and quartz veinlets are undeformed to weakly deformed with minor undulatory extinction observed in quartz.

JR-31 29-2 was hand-crushed and processed utilizing standard heavy liquid and magnetic separation techniques. Hundreds of zircon were obtained with sizes varying from <50 to ~100 μm in length. Individual zircons were mounted in epoxy, polished, and imaged in reflected light, backscattered light, and cathodoluminescence (CL). Sample preparation methods for ion probe analyses at the Stanford-USGS SHRIMP-RG facility follows those outlined in Schwartz et al. (2005).

3.1. U–Pb age determinations

Methods used to obtain the U–Pb analytical data closely follow those outlined by Compston et al. (1984) and Williams (1998), and are discussed in Schwartz et al. (2005). Samples were analyzed between 2005 and 2009 in multiple analytical sessions with standards run for every 3–4 unknowns. A gem-quality zircon, CZ3, with 550 ppm U was

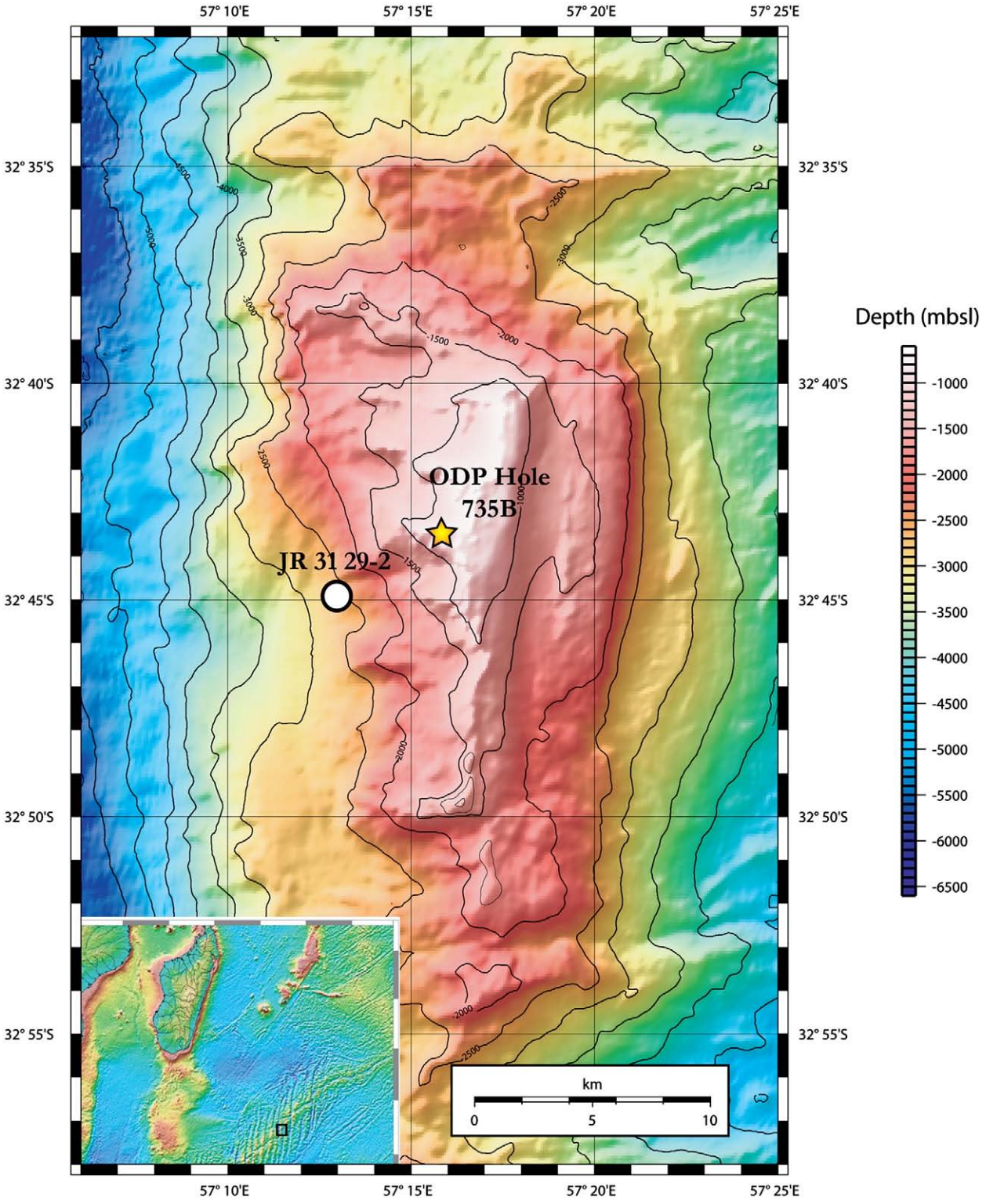

Fig. 1. Bathymetric map of Atlantis Bank depicting location of JR-31-29-2 (white circle) and ODP Hole 735B (yellow star).

used for U concentration determinations and grains of R33, a 419 Ma quartz diorite from the Braintree complex, Vermont was used as the Pb/U age standard (John Aleinikoff, personal communication, 2001). Raw data were reduced using SQUID (Ludwig, 2001) and all ages were calculated with Isoplot 3.00 (Ludwig, 2003). Corrections for common Pb in zircon were made following methods of Tera and Wasserburg (1972) using measured $^{207}Pb/^{206}Pb$ and $^{238}U/^{206}Pb$ ratios and an age-appropriate Pb isotopic composition of Stacey and Kramers (1975). Thorium-disequilibrium calculations were made following Schärer (1984) assuming Th/U of the magma = 3.0. Pb/U ages are reported in Table 1 and given at the 2σ level, unless otherwise noted. The ages reported here differ slightly from those reported by Schwartz et al. (2005) by $\leq$0.1 myr because additional age determinations were collected and Th-disequilibrium corrections are applied.

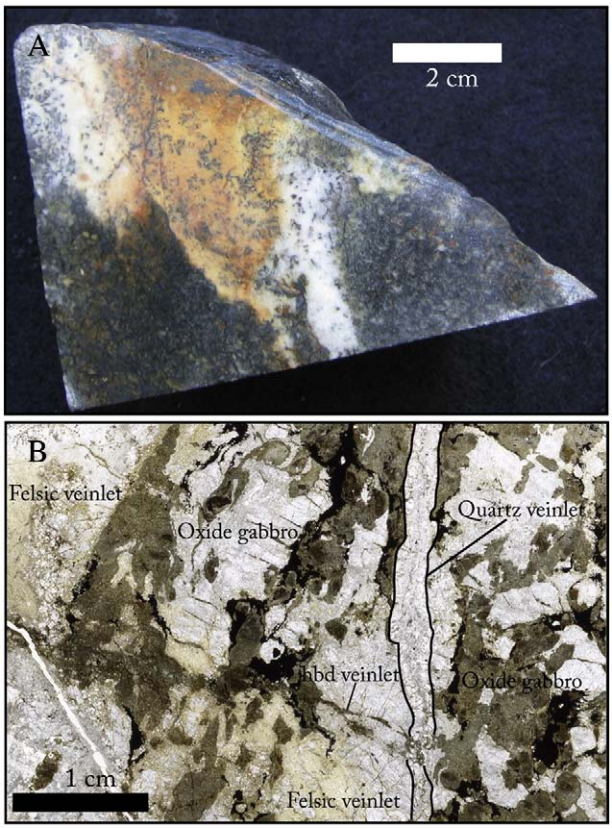

Fig. 2. A) Photograph of JR-31-29-2, an oxide gabbro cross-cut felsic vein and quartz vein and B) thin section scan of JR 31 29-2 showing cross-cutting felsic vein and quartz vein in oxide gabbro host rock. Zircons are located in the felsic vein, which contains plagioclase, quartz, clinopyroxene and titanite.

3.2. Trace element concentrations in zircon

Trace element analyses of zircon were also made with the U.S. Geological Survey-Stanford SHRIMP-RG between 2005 and 2009 (Claiborne et al., 2006; Mazdab and Wooden, 2006; Wooden et al., 2006). Methods closely follow those discussed by Mazdab (2009). SIMS analyses were performed using a 3–6 nA primary beam current and 15–20 μm spot size. Analyses collected in 2005 used a 30 μm spot size. Analyses dedicated to trace elements consisted of one block of 2 cycles. The consecutive cycles peak step sequentially from $^{9}Be^{+}$ to $^{254}UO^{+}$, and can be compared to check the reproducibility of raw counts during analysis of a single spot. The primary standard is a gem-quality crystal from Madagascar that has been extensively characterized in-house and found to be very chemically homogeneous. The secondary zircon is CZ3, a Sri Lankan zircon megacryst described by Ireland and Williams (2003). Slight compositional variations do exist in these natural materials and the range of values that we report reflect a combination of analytical effects and sample heterogeneity (see Supplementary Table 1 for standard values during analyses). Standards were run after every ten unknowns. For quantification of titanium concentrations, these natural standards were repeatedly analyzed against synthetic Ti-bearing zircons that have been independently characterized by electron microprobe analyses. The isotopes $^{48}Ti^{+}$ and $^{49}Ti^{+}$ are measured for comparison; $^{48}Ti^{+}$ is subject to more critical secondary ion beam interferences from $^{96}Zr^{+}$ and $^{48}Ca^{+}$, but these potential interferences are limited by the high mass resolution (M/ΔM and 11,000 at 10% peak height) of the SHRIMP-RG (Mazdab and Wooden, 2006). Ti-in-zircon temperatures listed in Table 1 were calculated using the less abundant isotope, $^{49}Ti^{+}$, though concentrations determined from either isotope are in close agreement. Calcium, Al, and Fe were measured after 2005 as tracers for identifying analyses where the ion beam may have unintentionally overlapped common inclusions.

Element/^{30}Si ratios are derived from the time-averaged counts for each mass for both the standards and unknowns, and values for unknowns are then compared to those of the primary standard to determine concentrations. The secondary standard provides an independent check of data quality. For P, Ti, and Y, 2σ precision is ±6%; for the measured REE (excluding La), Hf, Th, and U, 2σ precision ranges from ±8 to 18%; the precision for La is ±30%.

3.3. X-ray mapping and crystallographic misorientation of zircon

Qualitative analysis of inclusions was performed by energy-dispersive X-ray mapping of zircon using the JEOL 8600 electron microprobe at the University of Alabama. X-ray maps were acquired

Table 1
U–Pb SHRIMP isotopic analyses and ages for JR-31-29-2.

Spot	Texture[a]	Concentrations			Atomic ratios[b]				Age (Ma)	
		U (ppm)	Th (ppm)	Pb*[c] (ppm)	f_{206}[d] (%)	$^{238}U/^{206}Pb$[e] (err abs)	$^{207}Pb/^{206}Pb$[e] (err abs)	$^{206}Pb/^{238}U$[e] (err abs)	$^{206}Pb/^{238}U$[f] (1σ)	$^{206}Pb/^{238}U$[g] (1σ)
1.1	P	340	103	0.5	1.00	554.2±9.2	0.0542±45	0.00179±3	11.5±0.2	11.6±0.2
12.1	P	911	96	1.5	4.66	518.8±6.6	0.0831±9	0.00184±3	11.8±0.2	11.9±0.2
2.1	P	584	164	1.0	3.84	526.6±6.1	0.0766±33	0.00183±2	11.8±0.2	11.9±0.2
5.1	P	1035	231	1.7	2.48	522.7±4.5	0.0659±60	0.00187±2	12.0±0.1	12.1±0.1
9.1	P	1040	160	1.6	1.31	548.8±7.0	0.0567±28	0.00180±2	11.6±0.2	11.7±0.2
15.1	P	738	138	1.2	0.51	539.7±5.7	0.0503±24	0.00184±2	11.9±0.1	12.0±0.1
17.1	P	2022	201	3.3	1.27	528.4±4.1	0.0563±22	0.00187±2	12.0±0.1	12.1±0.1
10.1	WOZ	718	302	1.5	17.64	403.9±7.5	0.1857±89	0.00204±7	13.1±0.5	13.2±0.5
13.1	WOZ	342	115	0.6	2.29	495.2±8.3	0.0644±44	0.00197±4	12.7±0.2	12.8±0.2
08-2.1	WOZ	2191	228	3.8	0.52	500.4±0.8	0.0504±4	0.00199±2	12.8±0.1	12.9±0.1
08-3.1	WOZ	676	236	1.1	−0.01	506.5±1.4	0.0462±6	0.00197±3	12.7±0.2	12.8±0.2
08-4.1	WOZ	524	162	1.4	38.43	321.9±1.3	0.3499±3	0.00191±5	12.3±0.3	12.4±0.3
08-6.1	WOZ	388	68	0.7	5.37	498.5±1.9	0.0887±6	0.00190±4	12.2±0.2	12.3±0.2
08-7.1	WOZ	240	70	0.4	0.52	521.5±2.3	0.0504±11	0.00191±5	12.3±0.3	12.4±0.3
08-8.1	WOZ	228	66	0.4	5.15	498.5±2.4	0.0870±8	0.00190±5	12.3±0.3	12.4±0.3

[a] Textures based on cathodoluminescence images (Figs. 3 and 4): WOZ = weak-oscillatory zoning and P = porous domains.
[b] Errors are reported at 1σ level and refer to last digits.
[c] Radiogenic ^{206}Pb.
[d] Fraction of total ^{206}Pb that is common ^{206}Pb.
[e] Uncorrected ratios.
[f] ^{207}Pb corrected age.
[g] ^{207}Pb corrected age with Th-disequilibrium correction applied (assumes Th/U of magma = 3.0).

using a 15 kV accelerating voltage and 20–50 nA beam current. Electron backscatter diffraction patterns (EBSP) from the zircon grains were collected at the University of Wyoming using an HKL electron backscatter diffraction detector attached to a JEOL 5800LV SEM. Samples were tilted 70° to the incident beam and EBSPs were collected under low vacuum conditions using a WD of 26 mm and an accelerating voltage of 20 kV. Zircons from the original ion probe mount were mapped using beam scans with step sizes between 0.5 μm and 1 μm. The EBSPs were indexed automatically to determine crystallographic orientations, using HKL Channel 5 software. The resultant beam scans are presented as maps of relative crystallographic misorientation.

4. Results

4.1. Textural characteristics of zircons

4.1.1. Primary textures

Zircons from mafic rocks typically display sector and weak-oscillatory zoning (Tomaschek et al., 2003; McLelland et al., 2004; Bea et al., 2006; Grimes et al., 2007, 2009; Baines et al., 2009). Approximately 60% of all imaged zircons from JR 31 29-2 (Figs. 3, 4) preserve subtle, WOZ domains which are commonly restricted to interior and rim portions of zircon crystals (Fig. 3). Nearly all grains are overprinted by secondary textures characterized by cloudy porous regions in transmitted light and chaotic internal zonation features in CL (see discussion below).

4.1.2. Secondary textures

Secondary, non-igneous textures appear brighter in CL than WOZ domains in the same zircon (Fig. 4). In some cases, dark and light areas appear patchy or are randomly distributed. In these regions, there is no clear relationship to proximity to grain exteriors in the 2-D mount sections. However, these regions are strongly correlated with porous regions in BSE images (Figs. 4, 5). These micron- to submicron-scale pores may be voids, fluid/melt inclusions or regions of dissolution. In general, domains with limited or no porosity preserve oscillatory igneous zonation patterns, whereas regions with extensive porosity are characterized by chaotic patterns (c.f., Fig. 4). X-ray mapping of porous domains displays micron- to submicron-scale Y- and P-rich inclusions. Pores sometimes contain Fe-, Ca-, F- and Cl-rich inclusions. We do not observe magmatic resorption textures characterized by areas of embayed grain boundaries, or other evidence (e.g., luminescent rims) for the development of younger magmatic overgrowths.

4.2. Age relationship between primary and secondary zircons

A subset of fifteen zircon grains was analyzed to quantify the relationship between zircon zonation and the timing of crystallization and subsequent textural modification (Table 1). Individual U–Pb spot analyses are shown on Figs. 3, 4, and data are plotted on a Concordia diagram in Fig. 5. Based on textural information, we divide the zircon populations into two groups: WOZ domains which record older $^{206}Pb/^{238}U$ ages, and secondary (porous) domains which record younger ages (Figs. 3, 4, 6). WOZ domains yield a weighted-average $^{206}Pb/^{238}U$ age of 12.76 ± 0.20 Ma ($n = 8$, mswd = 1.5) (see inset in Fig. 5). This age is taken as the best estimate for the timing of igneous crystallization associated with the WOZ zircon population. This age also agrees with the lower intercept age for this population which yields an age of 12.70 ± 0.25 (mswd = 1.9). These ages differ slightly from the age reported in Schwartz et al. (2005), which used a smaller subset of data and applied the Sambridge and Compston (1994) deconvolution method (previously reported $^{206}Pb/^{238}U$ age: 12.48 ± 0.10). This method is described below as an alternatively viable age calculation and yields a similar age within error.

Porous zircon domains collectively yield a weighted-average $^{206}Pb/^{238}U$ age of 12.00 ± 0.16 Ma (n = 7, mswd = 1.7; inset Fig. 5). Statistically, the weighted-average age for all non-igneous textured zircons is younger than the WOZ zircon population, and is interpreted to date the timing of secondary textural development in these zircons. A less precise lower intercept age of 11.84 ± 0.37 Ma also overlaps the weighted-average age. These ages are similar to the age given in Schwartz et al. (2005) based on the Sambridge and Compston (1994) deconvolution method described below (previously reported $^{206}Pb/^{238}U$ age: 11.84 ± 0.10).

An alternative approach is to calculate ages for the WOZ and non-igneous zircon populations using the "mixture modeling" method of Sambridge and Compston (1994). The Sambridge and Compston "mixture modeling" method assumes *a priori* that the number of components is known (assumed here to be two: an igneous and a modified population) and the samples display a Gaussian distribution of ages. Using all analyses, the method produced $^{206}Pb/^{238}U$ ages of 12.03 ± 0.10 Ma (70% of zircon analyses) and 12.86 ± 0.17 Ma (30% of zircon analyses) for the two components. The age of the porous zircon population calculated by this method (12.03 ± 0.10 Ma) is identical to the weighted-average age for these zircons (12.00 ± 0.16 Ma). The weak-oscillatory-zoned population in the Sambridge and Compston method (12.86 ± 0.17 Ma) is slightly older than, but within error of, the calculated weighted-average age discussed above (12.76 ± 0.20 Ma). We prefer the weighted-average $^{206}Pb/^{238}U$ age calculations because they take into account the additional constraints provided by the textures of the grains; however both methods yield similar results.

4.3. Trace element characteristics

Trace element concentrations were collected to investigate the relationship between internal zonation textures, Pb/U age and chemistry (Tables 2, 3). Locations of trace element spot analyses are shown on Figs. 3, 4. We report concentrations of both trace elements (Ti, P, Y, Hf, U and Th) and rare earth elements (REEs) in Tables 2, 3. Analyses were performed on both WOZ and porous domains (Figs. 7–9). The average composition of oceanic zircons from gabbros exposed along the Mid-Atlantic Ridge and Southwest Indian Ridge is shown for reference (Grimes et al., 2009).

WOZ domains are characterized by extreme P (2611–9373 ppm) enrichment relative to porous domains (465–3145 ppm) and average oceanic zircon (~1050 ppm)(Fig. 6). Trivalent cations (e.g., REEs and Y) also display enrichment in WOZ domains relative to porous domains. This relationship is observed in the plot of molar ΣREEs + Y vs. molar P (Fig. 6) which displays a positive correlation, suggesting that the $REEs^{3+}$ and Y^{3+} are partially charged balanced by P^{5+} according to the 'xenotime'-coupled substitution [e.g., Speer, 1980b]. The best-fit array on this diagram has a slope of ~1.2, demonstrating a slight deficiency of P relative to the trivalent cations. Previous workers have recognized that the 'xenotime' exchange vector is not the exclusive substitution mechanism to account for the incorporation of trivalent cations in the zircon structure (Hinton and Upton, 1991; Maas et al., 1992; Hoskin et al., 2000; Finch et al., 2001; Hanchar et al., 2001; Finch and Hanchar, 2003; Hoskin and Schaltegger, 2003; Tomaschek et al., 2003). Other elements including Sc^{3+}, alkali and alkaline earths (not reported in this study), various transition elements and hydrous species may also substitute in the zircon structure and may account for the observed trend in these oceanic zircons (Speer, 1980b,a; Hoskin et al., 2000; Hanchar et al., 2001).

Rare earth element concentrations also decrease with Pb/U age from WOZ to porous domains (Fig. 6). WOZ domains are distinguished from porous domains by lower average chondrite-normalized $(Yb/Gd)_N$ values, higher chondrite-normalized $(Sm/La)_N$ values, larger Ce-anomalies, and higher average HREE concentrations (Fig. 7). Average $(Sm/La)_N$ for porous zircon domains is 55 (versus 835 in WOZ zircon domains), reflecting La enrichment in porous domains. Negative Eu anomalies characterize both WOZ and porous zircon; however, there is

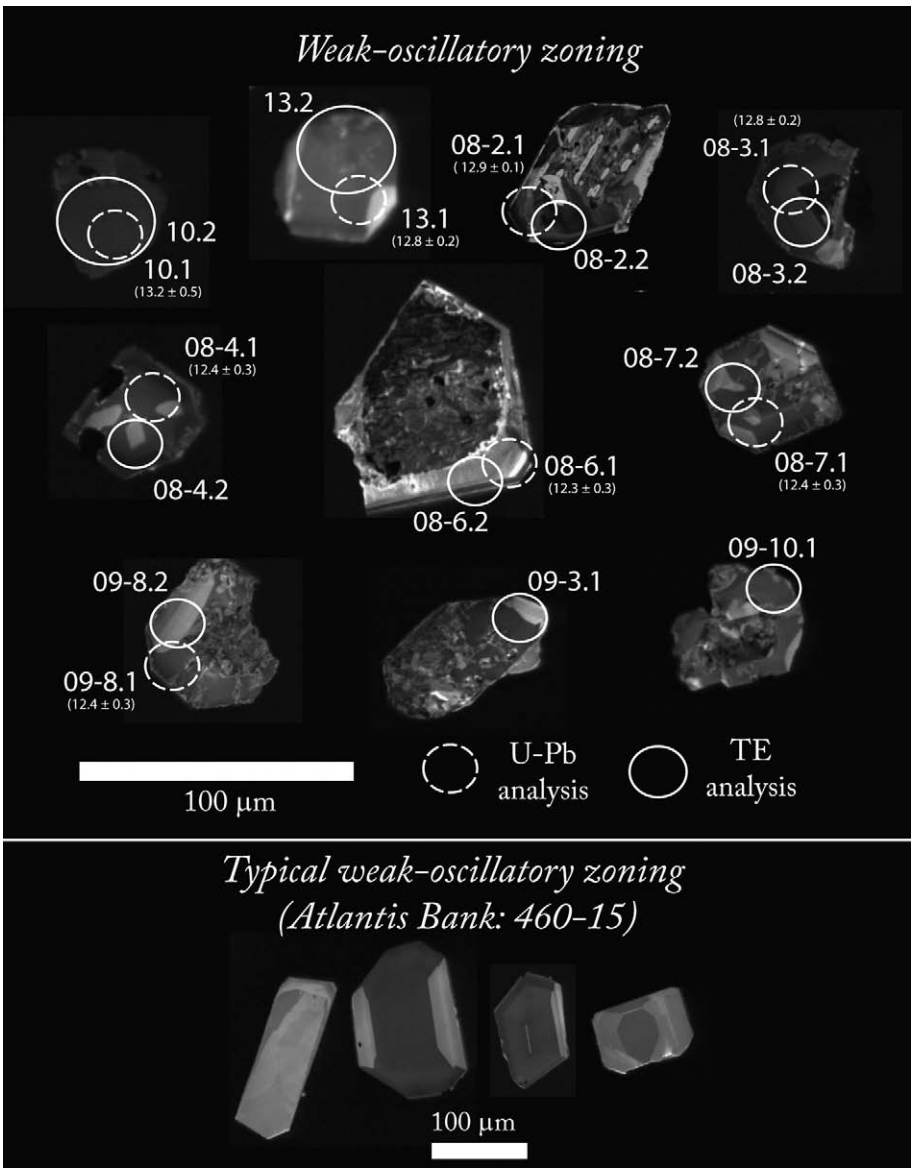

Fig. 3. Cathodoluminescence images of zircons which display weak-oscillatory-zoned zircon textures. Representative igneous zircons from other areas of Atlantis Bank (i.e., not from JR 31 29-2) are shown at the bottom for reference and also displaying weak-oscillatory-zoning textures. Dashed circles represent locations of U–Pb spot analyses; whereas solid circles represent locations of trace element spot analyses. $^{206}Pb/^{238}U$ ages are reported next to each U–Pb spot. Errors are reported at the 1σ confidence level.

no clear distinction between the two populations (Fig. 6). REE element patterns in WOZ and porous domains display heavy REE (HREE) enrichment relative to the light REEs (LREEs) as well as positive Ce and negative Eu anomalies (Fig. 7), similar to zircons reported in other studies (e.g., Maas et al., 1992; Hoskin et al., 2000; Hoskin and Schaltegger, 2003).

Concentrations of tetravalent cations are on average similar between WOZ domains and porous domains. Hf concentrations overlap between the two populations and are on average higher than average oceanic zircon. Similarly, Th and U values overlap, with WOZ domains extending to slightly higher concentrations in some cases. Corresponding Th/U values in WOZ zircons are on average slightly higher (0.31) than average porous zircons (0.22)(Fig. 6). Ti values largely overlap between the two populations (porous: 3.6–9.1 ppm; WOZ: 6.0–28.9 ppm) with two WOZ zircons extending to higher values (28 ppm), and porous domains extending to lowest values. Qualitative, uncorrected Ti-in-zircon temperatures of WOZ domains range from 856–699 °C with average value of 748 ± 58 °C (2SD of mean). Porous zircons yield a narrower range of uncorrected temperatures which range from 737 to 659, and an average value of 703 ± 55 °C.

4.4. Electron backscattered diffraction (EBSD) maps

Electron backscattered diffraction patterns have been used in recent studies to document the relationship between zircon crystallography and chemical changes due to high-temperature deformation and possible recrystallization (Hoskin and Black, 2000; Timms et al., 2006; Reddy et al., 2006, 2007, 2009). In an effort to evaluate whether the non-igneous internal textures and chemical variations we observe are controlled by deformation-related processes, we analyzed the crystallographic orientations of 10 zircons which preserve WOZ and non-igneous alteration/re-equilibration textures (a subset of 6 are shown in Figs. 9, 10). Maps of relative misfit of crystallographic orientation are shown for selected zircons in Figs. 9, 10. Misfit patterns reflect subtle changes in crystallographic orientation relative to a reference orientation (shown as '+' symbol in Figs. 9, 10). Most zircons display weak relative misfit patterns (<1°) that do not correlate with chemical zonation patterns observed in CL imaging (Figs. 9, 10). Some zircons display greater misorientations (up to 14%: Fig. 9a) that may indicate the presences of subgrain boundaries or minor fractures. Even in these zircons which have greater relative

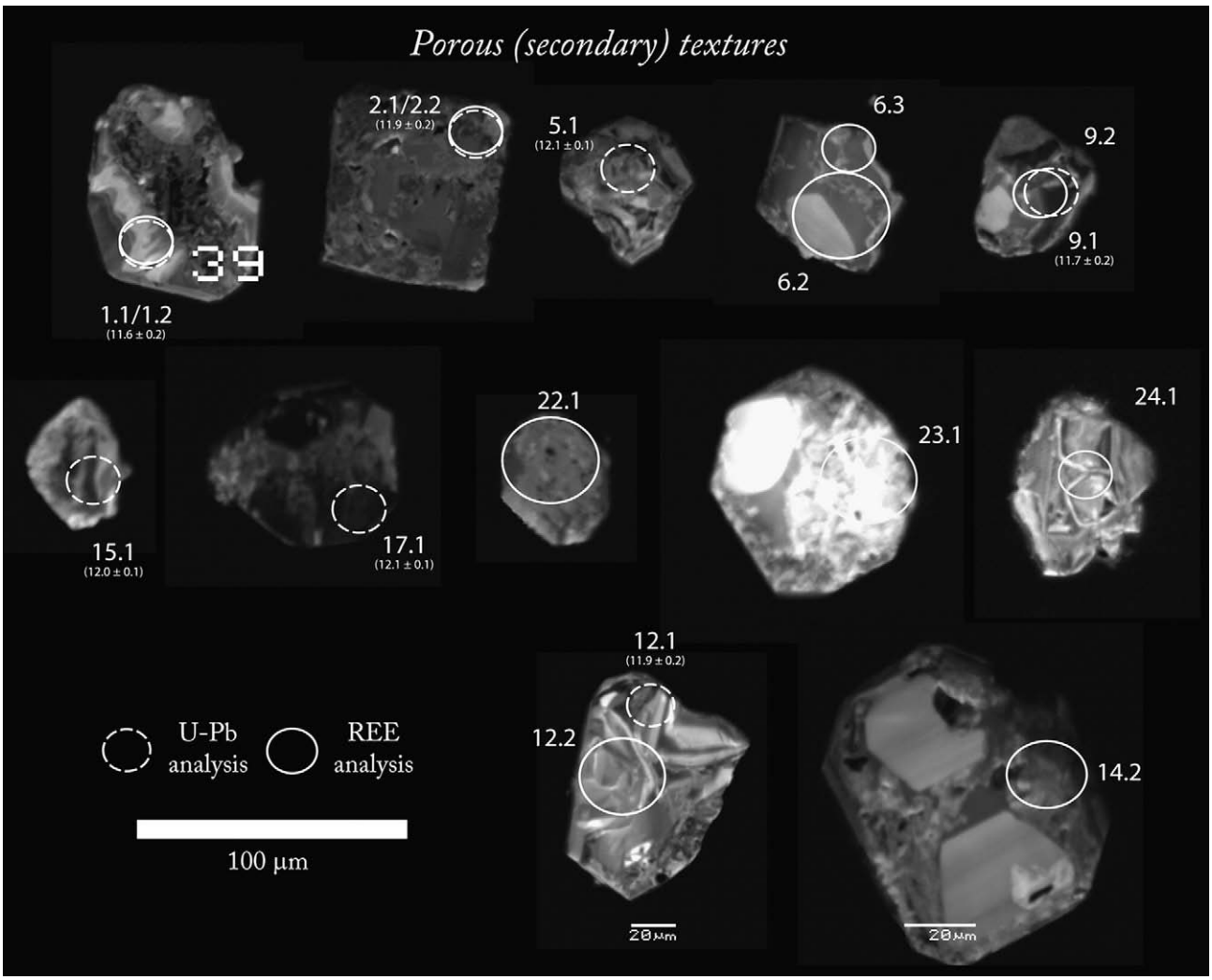

Fig. 4. Cathodoluminescence images of secondary (non-igneous) textures in zircons from JR 31 29-2. Dashed circles represent locations of U–Pb spot analyses; whereas solid circles represent locations of trace element spot analyses. $^{206}Pb/^{238}U$ ages are reported next to each U–Pb spot. Errors are reported at the 1σ confidence level.

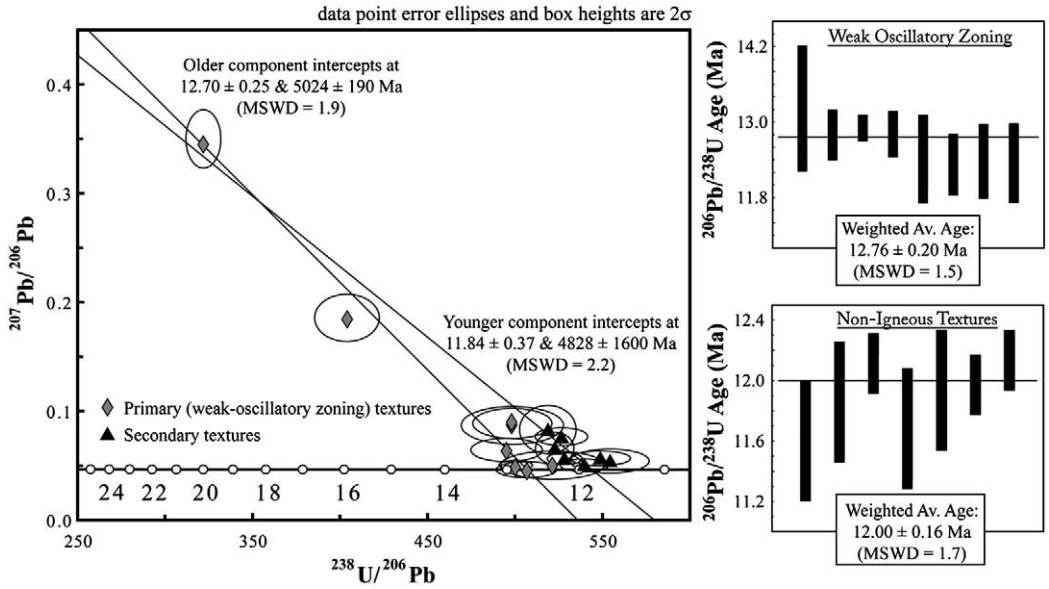

Fig. 5. Tera–Wasserburg diagram and weighted-average $^{206}Pb/^{238}U$ age plots. Ages for igneous and metamorphic components are calculated as weighted-average ages for both porous and WOZ igneous zircons. Best-fit regressions through both populations are also shown with calculated lower intercept age. Error ellipses and calculated ages are given at 2σ confidence level.

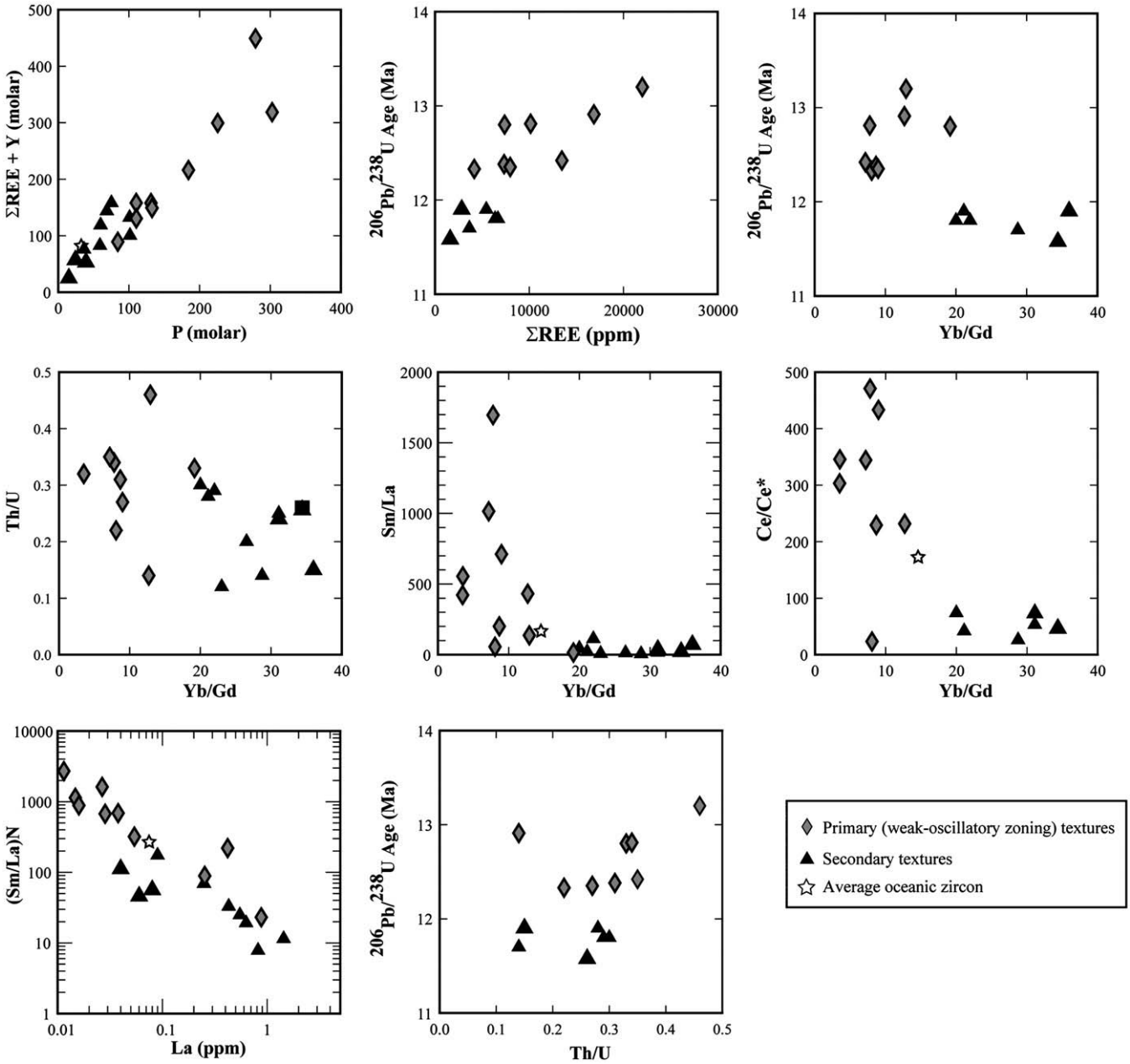

Fig. 6. Trivalent cations versus P geochemical plots for individual spot analyses showing the relationship between WOZ and porous domains. In general, WOZ igneous zircons have higher trace element concentrations relative to non-igneous zircons. Average composition of oceanic zircons from gabbros exposed along the Mid-Atlantic Ridge and Southwest Indian Ridge is shown for reference (Grimes et al., 2009).

misorientations, there does not appear to be a correlation with CL patterns and hence chemistry. Sharp relative misorientation boundaries of 4–5° occur over several microns in some zircons (e.g., Fig. 9). These features are linear in form and parallel to the *c*-axis. These planar low-angle misorientation boundaries may represent growth twins, or deformation-induced twins. Growth twins are not common in zircon, but are known to occur on [111] and [101] (Dana, 1916; Deer et al., 1978). Because the low-angle misorientation boundaries shown in Fig. 9 are parallel to the *c*-axis, they cannot be [111] or [101]. Deformation twins are also not common in zircon and have mostly been reported in shocked zircons (Bohor et al., 1993; Krogh et al., 1993; Kamo et al., 1995; Leroux et al., 1999). Most important for this study, there is no correlation between these probable twins and crystal chemistry, suggesting that intracrystalline deformation did not play a significant role in the development of non-igneous alteration/re-equilibration textures and associated chemical variations.

5. Discussion

5.1. Mechanisms of textural development and chemical variation

Our observations of internal textural features, Pb/U ages, trace element and REE geochemistry, and X-ray and EBSD maps allow us to evaluate changes in the character of oceanic zircons with respect to original igneous crystallization and subsequent modification. Textures similar to those we describe have been reported from magmatic zircons, which have experienced hydrothermal fluid alteration and/or high-temperature/pressure metamorphic conditions (Pidgeon, 1992; Nemchin and Pidgeon, 1997; Hoskin and Black, 2000; Corfu et al., 2003; Tomaschek et al., 2003; Puga et al., 2005). The development of porous domains truncating primary growth zones is thought to develop by secondary alteration and/or re-equilibration processes, possibly promoted by the presence of aqueous fluids (Pidgeon, 1992;

Table 2
Trace element analyses (SHRIMP-RG) of zircon from JR 31 29-2.

Sample[a]	12.2	24.1	2.2	6.2	6.3	9.2	14.2	22.1	23.1	1.2	10.2
Texture[b]	P	P	P	P	P	P	P	P	P	P	WOZ
La (ppm)	0.04	0.08	0.43	0.09	0.25	0.82	0.55	1.44	0.63	0.06	0.42
Ce (ppm)	29.2	26.6	43.0	49.3	61.2	34.7	61.9	36.9	29.3	14.3	210.8
Pr (ppm)	0.00	0.10	0.14	0.00	0.16	0.13	0.14	0.00	0.00	0.08	0.00
Nd (ppm)	0.8	0.7	3.6	2.8	4.1	1.6	3.2	7.8	5.7	0.7	15.3
Sm (ppm)	2.8	2.8	8.8	10.0	10.9	4.0	8.5	10.3	7.6	1.8	57.3
Eu (ppm)	0.2	2.5	1.1	1.0	1.1	0.3	0.7	0.9	0.6	0.1	1.7
Gd (ppm)	38	44	108	131	132	57	116	82	88	22	652
Tb (ppm)	18	20	47	56	58	25	55	31	36	10	257
Dy (ppm)	256	299	639	778	787	373	774	407	503	148	3327
Ho (ppm)	118	132	283	339	333	171	364	160	196	67	1290
Er (ppm)	595	691	1314	1547	1538	820	1774	797	1009	359	5294
Tm (ppm)	155	163	292	357	337	197	421	211	261	89	1114
Yb (ppm)	1365	1365	2282	2885	2646	1650	3604	1876	2348	749	8434
Lu (ppm)	253	246	416	514	462	315	669	350	459	143	1342
ΣREE (ppm)	2830	2992	5438	6669	6371	3651	7853	3971	4945	1603	21997
Hf (ppm)	22576	20178	17126	20211	13257	21322	16434	27669	19415	17440	20261
Th (ppm)	90	120	114	96	61	60	222	212	78	34	418
U (ppm)	594	509	400	330	207	427	892	1751	382	132	916
Y (ppm)	3226	3489	7699	8238	9412	4819	9934	5256	6315	1706	28326
P (ppm)	1217	752	1855	3125	2131	1132	2332	1829	3145	465	8643
Ti (ppm)	3.7	5.5	6.3	8.6	8.0	6.5	7.8	9.1	6.8	3.6	28.9
Th/U	0.15	0.24	0.28	0.29	0.30	0.14	0.25	0.12	0.20	0.26	0.46
Ce/Ce*	n.d.	73	42	n.d.	74	26	53	n.d.	n.d.	49	n.d.
Eu/Eu*	0.07	0.70	0.10	0.08	0.09	0.07	0.07	0.10	0.07	0.05	0.03
P (molar)	39	24	60	101	69	37	75	59	102	15	279
ΣREE (molar)	17	18	32	39	38	22	46	23	29	9	131
Y (molar)	36	39	87	93	106	54	112	59	71	19	319
(Sm/La)N	111	56	33	174	69	8	25	11	19	48	220
(Yb/Gd)N	44	38	25	27	24	35	38	28	32	42	16

[a] Average zircon from Grimes et al. (2009).
[b] P = porous and WOZ = weak-oscillatory zoned.
[c] Ti-in-zircon temperature calculated after Watson and Harrison (2005).

Nemchin and Pidgeon, 1997; Schaltegger et al., 1999; Corfu et al., 2003; Geisler et al., 2007). Mechanisms for alteration and re-equilibration of zircon may include coupled dissolution–reprecipitation (Tomaschek et al., 2003; Geisler et al., 2007), diffusion–reaction–re-equilibration facilitated by the presence of an aqueous fluid (Geisler et al., 2003a,b, 2007), static grain-boundary and defect migration (Hoskin and Black, 2000), and/or deformation-enhanced diffusion along high diffusivity pathways (Timms et al., 2006; Reddy et al., 2006, 2009). One or more of these processes may explain the textural features we observe as well as the apparent relationship between micro-porosity and mottled regions in these oceanic zircons.

Re-equilibration processes may have the effect of either purging or adding non-essential structural constituent cations to the zircon lattice (c.f., Geisler et al., 2007). Depending on the mechanism of alteration, cations with ionic radii significantly different from essential structural constituent cations (Si, Zr and Hf) may be preferentially expelled from the zircon lattice (Hoskin and Black, 2000; Geisler et al., 2007), resulting in lower overall concentrations. In some cases, trace element impurities may be concentrated in mottled and convoluted regions of the crystal (e.g., Pidgeon et al., 1998). Our results are consistent with earlier studies of texturally altered zircons and suggest that development of micro-porosity and secondary internal zonation features at approximately 12.0 Ma resulted in the expulsion of non-essential cations (Y, P, REEs, and Pb* [radiogenic Pb]) during alteration/re-equilibration under amphibolite-facies conditions. Removal of non-essential structural constituent cations is likely responsible for the correlation between Pb/U ages, decreasing REE, Y and P concentrations, and Th/U values in porous domains. Below we explore mechanisms by which these zircons may have undergone alteration/re-equilibration, and implications for trace element mobility in gabbroic ocean crust.

Mechanisms of modification in igneous zircon may involve either fluid-dominated or solid-state re-equilibration (static or dynamic). In both cases the driving force is either a reduction of lattice strain resulting from high concentrations of trace elements in solid solution (e.g., Hoskin and Black, 2000; Tomaschek et al., 2003), or in metamict zircons, recovery of structural damage caused by self-irradiation (Chakoumakos et al., 1987; Murakami et al., 1991; Geisler et al., 2003b). Because these zircon are <13 Ma, calculated α-decay doses over this time are well below the critical value of 3×10^{15} α-decay events/mg for detectable decay damage (Murakami et al., 1991). Therefore, radiation damage is unlikely to have significantly influenced chemical behavior of these zircons during secondary alteration. However, these zircons are highly enriched in trace elements (compare with average oceanic zircons in Fig. 6; Tables 2, 3), resulting in significant internal lattice strain. In the case of solid-state re-equilibration, dissipation of structural stress caused by the incorporation of trace element 'impurities' is accomplished by cation and defect migration (e.g., Hoskin and Black, 2000). Some have argued that diffusion along high diffusivity pathways may also result in trace element migration during solid-state dynamic re-equilibration (Timms et al., 2006; Reddy et al., 2006, 2009). In contrast, fluid-dominated re-equilibration can occur by coupled dissolution–reprecipitation (O'Neil and Taylor, 1967; Putnis, 2002; Tomaschek et al., 2003; Geisler et al., 2007). In considering the applicability of these mechanisms to the re-equilibration of zircons in JR-31 29-2, we first consider the case of solid-state re-equilibration by volume diffusion.

Volume diffusion by interstitial vacancy mechanism is the primary means by which trace elements diffuse through zircon (e.g., Cherniak et al., 2003). Volume diffusion has been studied extensively for a number of trace elements (U, Th, REEs, Pb, and Ti) in both natural and synthetic zircons (Cherniak et al., 1997b,a; Lee et al., 1997; Hanchar et al., 2001; Cherniak et al., 2003; Cherniak and , 2006). In order to qualitatively examine the degree to which variations in chemistry and CL textures can be accounted for by volume diffusion, we calculate diffusion distances for

13.2	08-2.2	08-3.2	08-4.2	08-6.2	08-7.2	08-8.2	09-3.1	09-10.1	Average	Average	Average
WOZ	WOZ	WOZ	WOZ	WOZ	WOZ	WOZ	WOZ	WOZ	Porous	WOZ	Ocean zircon
0.88	0.04	0.01	0.03	0.25	0.05	0.01	0.03	0.02	0.44	0.17	0.08
91.8	90.9	110.8	155.0	41.8	81.5	81.7	78.0	70.5	38.6	101.3	77.8
0.00	0.23	0.28	0.44	0.73	0.13	0.14	0.13	0.15	0.07	0.22	0.16
3.6	3.9	5.2	7.6	9.1	2.8	2.8	3.1	2.5	3.1	5.6	4.3
12.7	16.3	19.5	27.0	14.2	10.8	10.5	12.0	8.9	6.8	18.9	12.2
1.3	0.3	1.8	2.5	0.3	1.1	0.9	1.2	1.0	0.9	1.2	2.4
162	218	242	323	118	145	152	153	131	82	270	135
69	108	102	133	43	64	67	66	57	36	113	34
959	1709	1248	1793	568	861	999	876	797	496	1159	626
374	657	538	757	210	363	380	370	318	216	624	174
1681	3399	2447	3220	970	1726	1856	1725	1533	1045	2385	1164
387	879	522	684	208	378	413	377	336	248	530	165
3100	8344	4194	5435	1693	3148	3416	3058	2807	2077	4363	1977
545	1442	709	920	287	548	594	536	483	383	741	213
7387	16868	10140	13458	4164	7329	7973	7256	6544	4632	10311	4584
18473	25653	17054	15738	22793	16652	16951	15433	16933	19563	18594	12195
149	405	163	189	87	95	91	89	102	109	179	312
457	2892	473	540	389	304	336	276	314	562	690	299
10159	19495	13883	19529	5733	9453	9829	9414	8158	6009	13398	4600
3417	9373	5706	6990	2611	4103	4067	4111	3421	1798	5244	1051
28.7	5.9	8.5	10.7	6.1	7.9	7.2	7.9	7.9	6.6	12.0	21.5
0.33	0.14	0.34	0.35	0.22	0.31	0.27	0.32	0.32	0.22	0.31	1.04
n.d.	232	471	344	23	229	433	303	346	53	298	171
0.09	0.01	0.08	0.08	0.02	0.08	0.07	0.06	0.06	0.14	0.06	0.18
110	303	184	226	84	132	131	133	110	58	169	34
44	99	60	80	25	43	47	43	39	27	61	27
114	219	156	220	64	106	111	106	92	68	151	52
23	688	2704	1618	89	320	1134	673	885	55	835	257
23	46	21	20	17	26	27	10	11	33	22	18
856	699	730	753	701	724	717	725	724	705	748	806

Dy and Yb at the temperatures (~650 °C) appropriate for these zircons. Empirically-derived volume diffusion parameters for REEs (Cherniak et al., 1997b) over 12.0 myr yield diffusion distances of 0.016 and 0.110 nm for Dy and Yb, respectively. However, timescales of cooling in slow-spreading lower oceanic crust are <1 myr (over temperature range of 800–200 °C: John et al., 2004; Schwartz et al., 2009), resulting in diffusion distances of 0.005 and 0.031 nm for Dy and Yb respectively. These calculations indicate that volume diffusion is simply too slow even at amphibolite-facies conditions over these timescales to account for the chemical heterogeneity we observe associated with secondary textural development. Solid-state chemical mobility along high diffusivity pathways (e.g., Timms et al., 2006; Reddy et al., 2006, 2009) is also highly unlikely because crystallographic misfit features do not correlate with the internal chemical zonation patterns (Figs. 8, 9).

Coupled dissolution–reprecipitation is an alternative process whereby zircons which are out of equilibrium (due to changes in temperature and/or pressure) with a co-existing fluid phase are dissolved and reprecipitated such that chemical equilibrium between the zircon and the hydrothermal fluid is established (Tomaschek et al., 2003). The driving force behind the dissolution–reprecipitation reaction is the reduction of free energy associated with the removal of 'impurities' from the crystal lattice (Putnis, 2002). During this process, the unstable trace element-enriched zircon is dissolved into the fluid and reprecipitated directly on the reaction interface in the same crystallographic orientation as the original zircon (Tomaschek et al., 2003), a relationship supported by our EBSD data (e.g., Figs. 8, 9). As the reaction front progresses, porosity is created and maintained within the zircon, allowing contact between the advancing reaction front and the external fluid. Preservation of this process is observed in fluid inclusions, pits and internal porous skeletal structures (Geisler et al., 2003a; Tomaschek et al., 2003; Puga et al., 2005).

Dissolution–reprecipitation has been invoked to explain texturally and chemically altered trace element-enriched zircons in high-pressure, low-temperature rocks from Syros, Greece which display mottled zonation patterns and the development of secondary porosity (up to 10%) (Tomaschek et al., 2003). Dissolution–reprecipitation processes in these rocks occurred by the unbalanced reaction (Zr, Hf, Y, REE)(Si, P)$O_4 \rightarrow$ (Zr,Hf)SiO4 + (Y,REE)PO_4 at temperatures of ~480 °C (Pan, 1997; Tomaschek et al., 2003). A key feature of these zircons is the association of porous regions with trace element-enriched inclusions, which represent the precipitates of elements no longer compatible in the zircon lattice. A component of the incompatible trace elements may also be lost to the fluid. Geisler et al. (2007) discuss the relationship between pores and trace element-enriched inclusions in terms of a thermodynamic model of a solid solution–aqueous solution system in which trace element-rich zircon has a greater solubility in an aqueous fluid relative to pure zircon end member. In this solid solution–aqueous solution system, a eutectic point exists between trace element poor zircon and trace element-enriched inclusions (e.g., xenotime) such that during the interfacial dissolution–reprecipitation process, the aqueous fluid may coexist in equilibrium with a trace element poor zircon and trace element-enriched phase. Geisler et al. (2007) note that the coupled dissolution–reprecipitation reaction results in secondary porosity, volume loss (to the aqueous fluids), and may or may not result in the precipitation of trace element-enriched inclusions depending on whether or not the eutectic point of the solid solution–aqueous solution system is reached.

In zircons from JR-31-29-2, we observe many of the features characteristic of coupled dissolution–reprecipitation process, including: 1) the development of secondary micro-porosity associated with mottled, convolute and wavy domains, 2) the consistency of crystallographic orientation between non-igneous (mottled, convoluted and wavy) and WOZ regions, and 3) micron- to submicron-scale P- and Y-rich inclusions in some but not all porous zircon domains. We also

observe that concentrations of REEs, Y and P are extremely enriched in older WOZ domains relative to younger porous regions, occurring at concentrations much higher than average oceanic zircons. Porous zircons tend to have lower trace element concentrations which cluster around average oceanic zircon values and show a more restricted compositional range. Porous zircons also display low average chondrite-normalized $(Sm/La)_N$ and lower average Th/U values (Fig. 6), features which have been reported in other studies of altered zircons and have been interpreted to indicate interaction with hydrothermal fluids (Hoskin et al., 1998; Whitehouse and Kamber, 2002; Hoskin, 2005; Grimes et al., 2009). Alternatively, these features may also be attributed to initial chemical variations created during igneous crystallization followed by deuteric alteration. We view this scenario as unlikely because WOZ and porous domains are separated in time by 760 ± 360 kyr, which, given documented cooling rates from Atlantis Bank of ~800 °C/myr (John et al., 2004; Schwartz et al., 2009) precludes simple deuteric alteration associated with monotonic cooling. Furthermore, REE, Y and P concentrations negatively correlate with Pb/U age, and are consistent with a younger event affecting internal textures, U–Pb isotopic systematics and trivalent cation concentrations.

5.2. Implications for the geochemistry and geochronology of lower oceanic crust

Zircons from JR 31 29-2 display an age distribution that cannot be explained by simple igneous crystallization of a homogenous population. The weighted-average age of protolith, WOZ zircons (12.76 ± 0.20 Ma) is ~1 myr older than the local sea surface magnetic age where the rock was obtained (~11.75 Ma:, Baines et al., 2008) and its age range (1.6 ma) is significantly different than predicted by conventional models for crustal accretion at mid-ocean ridges (ca. 100,000–200,000: Meurer and Gee, 2002; Grimes et al., 2008; Baines et al., 2009; Lissenberg et al., 2009). Hence, these zircons are anomalously old and may represent xenocrysts of an older rock which were entrained in the late-stage felsic vein. Other anomalously old Pb/U zircon ages from Atlantis Bank have been discussed by Schwartz et al. (2005) and may represent either 1) crustal blocks trapped by stochastic intrusion processes within the lower oceanic crust, or 2) gabbroic bodies which originally crystallized at depth in the axial mantle lithosphere and were later assimilated at shallow levels during accretion of Atlantis Bank.

In the porous textural domains, we do not observe evidence of magmatic resorption features or secondary magmatic rims; instead, the younger ages are associated with internal alteration textures and secondary micro-porosity, which may record an episode of coupled dissolution–reprecipitation facilitated by migrating aqueous fluids as discussed above. The quartz, albite and hornblende veinlets which cross-cut the felsic vein may record this episode of alteration and fluid migration through the rock. The age of these zircons is similar within error to the sea surface magnetic age for the portion of crust where JR-31 29-2 was collected (~11.75 Ma:, Baines et al., 2008) and is similar to other ages reported from the area (John et al., 2004; Schwartz et al., 2005; Baines et al., 2009). Given the local availability of mafic magmatism and associated deuteric and hydrothermal fluids during the construction of oceanic crust at this time (e.g., Hart et al., 1999), it is plausible that the development of the non-igneous, alteration/re-equilibration textures are related to a short-lived (<1 myr) hydrothermal pulse associated with the creation of this portion of Atlantis Bank at approximately 12.0 Ma.

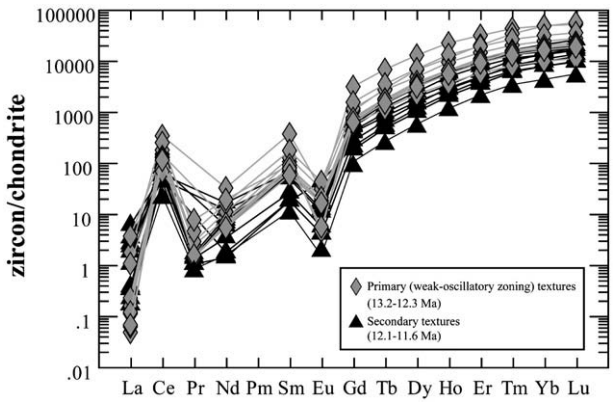

Fig. 7. Rare earth element patterns for selected zircons which also have corresponding $^{206}Pb/^{238}U$ ages. Patterns are displayed in order of decreasing age, with Th corrected $^{206}Pb/^{238}U$ age range. The general pattern we observe suggests decreasing REE contents with decreasing age.

Coupled dissolution–reprecipitation in association with aqueous fluids during a high-temperature thermal event best describes many aspects of the textural and chemical development of these altered zircons. During this process, newly precipitated zircons will on average contain less minor and trace elements than the parent zircons, including both radiogenic and common Pb (e.g., Tomaschek et al., 2003). In terms of geochronology, the U–Pb isotopic system in the newly re-equilibrated zircon domains will be effectively reset by the dissolution–reprecipitation process because Pb^{2+} will be strongly excluded from the zircon lattice during reprecipitation (e.g., Geisler et al., 2007). Analysis of the reprecipitated domains should therefore date the timing of metamorphism and fluid-induced re-equilibration. Supporting this assertion are the similarities in age between the non-igneous, alteration/re-equilibration textures in JR 31-29-2 and sea surface magnetic ages (Dick et al., 1991b; Hosford et al., 2003; Baines et al., 2008) and other Pb/U zircon ages from the area (John et al., 2004; Schwartz et al., 2005; Baines et al., 2009).

5.3. Comparison to porous zircons from disrupted oceanic crust

Porous zircon development is also reported from on-land ophiolites and disrupted portions of oceanic crust (e.g., Rubatto and Hermann, 2003; Spandler et al., 2004; Liati et al., 2005; Puga et al., 2005). Protolith zircons in these studies are characterized by elevated concentrations of trace elements, magmatic Th/U rations, igneous REE patterns and weak-oscillatory zonation patterns in CL. In contrast, hydrothermally altered igneous zircons display mottled textures, which are often associated with porosity and trace element-enriched inclusions. These mottled zircons also display evidence for Pb loss and lower overall concentrations of HREE. Temperature conditions for hydrothermal alteration are often obscured by later metamorphic overprinting reactions (e.g., Puga et al., 2005), but are documented by low-T, low-P assemblages armored within some zircons (<100 °C, <0.2 GPa: Spandler et al., 2004). These metamorphic temperatures as well as those reported in this study and in Tomaschek et al. (2003) may suggest that hydrothermal alteration of igneous zircons can occur over a variety of temperatures. These zircons from disrupted oceanic crustal rocks display remarkable similarity to zircons reported in this study from Atlantis Bank, and provide evidence for both the presence of igneous zircons in oceanic crust and their alteration by hydrothermal fluids on the seafloor. The preservation of mottled and re-equilibrated textures in JR 31 29-2 offers an in-situ example of seafloor metamorphism and re-equilibration of igneous zircons and represents a snapshot in time of fluid-dominated re-equilibration processes which did not continue to completion.

Acknowledgements

We thank Henry Dick for access to samples from the James Clark Ross cruise. We gratefully thank Drs. Geisler, Hoskins and Rudnick for thorough and helpful reviews. Funding for this work was provided by a Wyoming NASA Space Grant and University of Alabama start-up funds to Schwartz and a NSF OCE grant #0352054 to Cheadle and John.

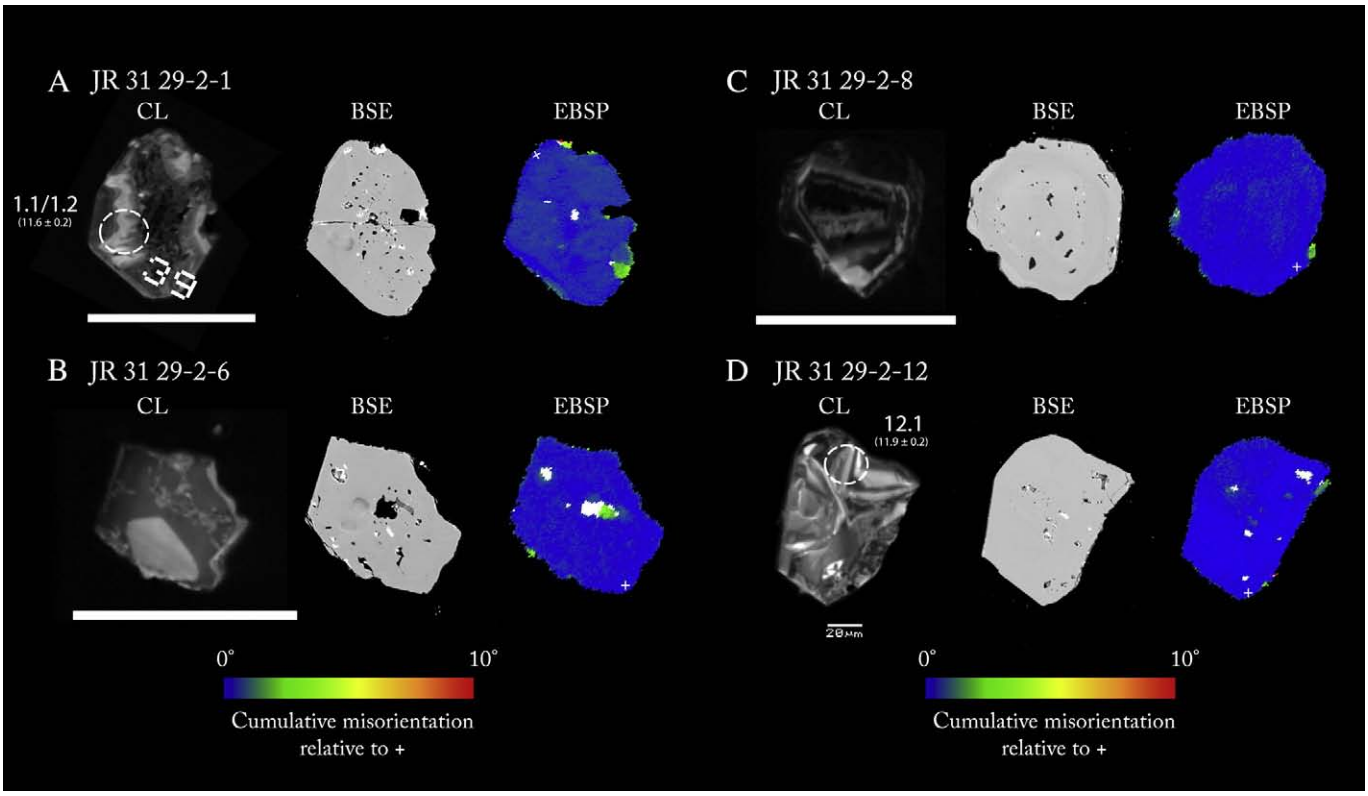

Fig. 8. Relationship between internal zonation texture (cathodoluminescence images), development of secondary porosity (backscattered electron images) and relative misorientation (electron backscattered diffraction maps). Scale bars are 100 µ, with the exception of 'd'.

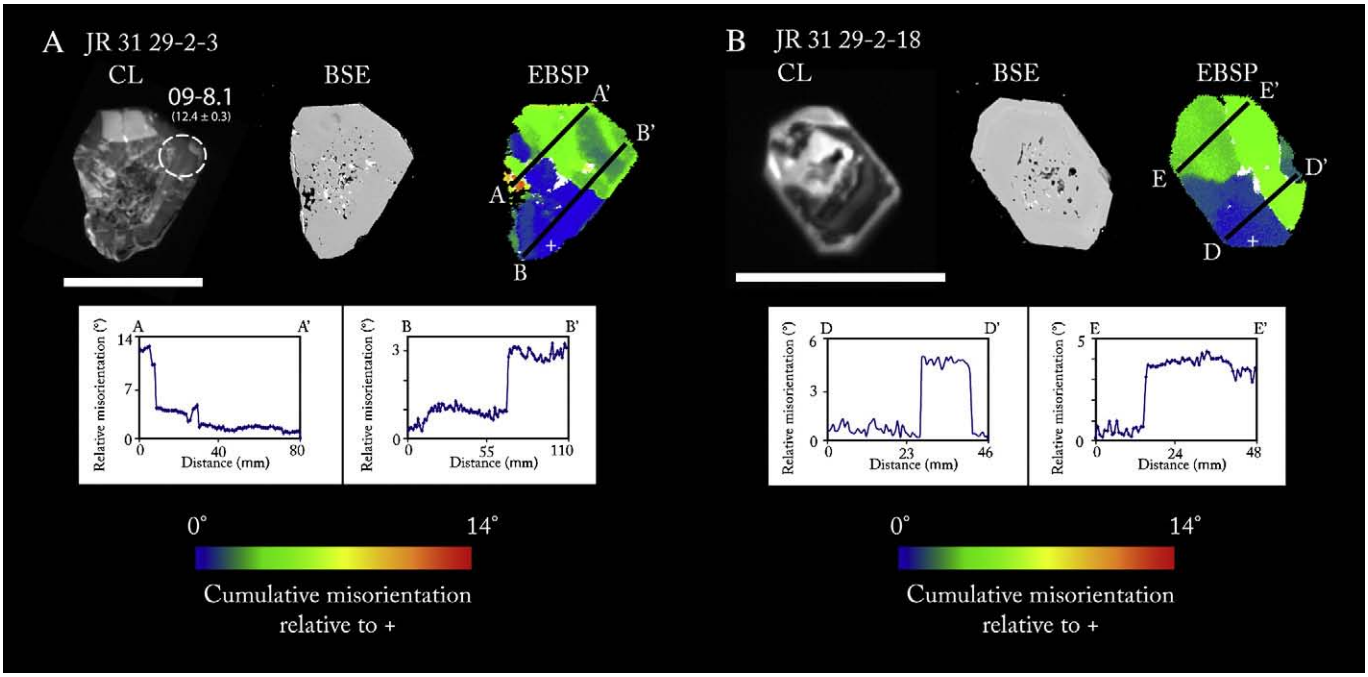

Fig. 9. Relationship between internal zonation texture (CL images), development of secondary porosity (BSE images) and relative misorientation for zircons. Low-angle-misorientation boundaries in these zircons may indicate slight amounts deformation, or growth twinning. Importantly, there is no relationship between this possible deformation and internal zonation patterns. The shape of zircon in 'b' is slightly different between the CL image and the BSE image and the misorientation map because subsequent polishing revealed tips that were previously unexposed beneath epoxy.

Appendix A. Supplementary data

Supplementary data associated with this article can be found, in the online version, at doi:10.1016/j.chemgeo.2010.03.017.

References

Baines, A.G., Cheadle, M.J., Dick, H.J.B., Hosford Scheirer, A., John, B.E., Kusznir, N.J., Matsumoto, T., 2007. The evolution of the Southwest Indian Ridge from 55°45′E–62°E: changes in plate-boundary geometry since 26 Ma. Geochemistry Geophysics Geosystems 8, Q06022. doi:10.1029/2006GC001559.

Baines, A.G., Cheadle, M.J., John, B.E., Schwartz, J.J., 2008. The rate of oceanic detachment faulting at Atlantis Bank, SW Indian Ridge. Earth and Planetary Science Letters 273, 105–114. doi:10.1016/j.epsl.2008.06.013.

Baines, A.G., Cheadle, M.J., John, B., Grimes, C.B., Schwartz, J.J., Wooden, J.L., 2009. SHRIMP Pb/U zircon ages constrain gabbroic crustal accretion at the ultraslow-spreading Southwest Indian Ridge. Earth and Planetary Science Letters 287, 540–550.

Bea, F., Montero, P.G., Gonzalez-Lodeiro, F., Talavera, C., Molina, J.F., Scarrow, J.H., Whitehouse, M.J., Zinger, T., 2006. Zircon thermometry and U–Pb ion-microprobe dating of the gabbros and associated migmatites of the Variscan Toledo Anatectic Complex, Central Iberia. Journal of the Geological Society 163, 847–855.

Bohor, B.F., Betterton, W.J., Krogh, T.E., 1993. Impact-shocked zircons; discovery of shock-induced textures reflecting increasing degrees of shock metamorphism. Earth and Planetary Science Letters 119, 419–424.

Cannat, M., Mevel, C., Stakes, D.S., Von Herzen, R.P., Robinson, P.T., Adamson, A.C., Becker, K., Bloomer, S.H., Dick, H.J.B., Emmermann, R.F.K., Gard, G., Goldberg, D., Hebert, R., Hertogen, J.G.H., Hoskins, H., Iturrino, G., Kassenaar, J.D.C., Kempton, P.D., Kikawa, E., Kirby, S.H., Meyer, P.S., Natland, J.H., Ozawa, K., Pariso, J., Scott, J.H., Swift, S.A., 1991a. Normal ductile shear zones at an oceanic spreading ridge; tectonic evolution of Site 735 gabbros (Southwest Indian Ocean). Proceedings of the Ocean Drilling Program, Scientific Results 118, 415–429.

Cannat, M., Von Herzen, R.P., Robinson, P.T., Adamson, A.C., Becker, K., Bloomer, S.H., Dick, H.J.B., Emmermann, R.F.K., Gard, G., Goldberg, D., Hebert, R., Hertogen, J.G.H., Hoskins, H., Iturrino, G., Kassenaar, J.D.C., Kempton, P.D., Kikawa, E., Kirby, S.H., Meyer, P.S., Natland, J.H., Ozawa, K., Pariso, J., Scott, J.H., Stakes, D.S., Swift, S.A., 1991b. Plastic deformation at an oceanic spreading ridge; a microstructural study of the Site 735 gabbros (Southwest Indian Ocean). Proceedings of the Ocean Drilling Program, Scientific Results 118, 399–408.

Cannat, M., Karson, J.A., Miller, D.J. (Eds.), 1995. Proceedings of the Ocean Drilling Program Initial Reports Leg 153. Ocean Drilling Program, College Station, TX. 798 pp.

Chakoumakos, B.C., Murakami, T., Lumpkin, G.R., Ewing, R.C., 1987. Alpha-decay-induced fracturing in zircon; the transition from the crystalline to the metamict state. Science 236, 1556–1559.

Cherniak, D.J., Watson, E.B., 2006. Ti diffusion in zircon. Fall Meeting Supplement: Eos Trans. AGU, 87. V31F-02.

Cherniak, D.J., Hanchar, J.M., Watson, E.B., 1997a. Diffusion of tetravalent cations in zircon. Contributions to Mineralogy and Petrology 127, 383–390.

Cherniak, D.J., Hanchar, J.M., Watson, E.B., 1997b. Rare-earth diffusion in zircon. Chemical Geology 134, 289–301.

Cherniak, D.J., Watson, E.B., Watson, E.B., Cherniak, D.J., 2003. Diffusion in zircon. Reviews in Mineralogy and Geochemistry 53, 113–143.

Claiborne, L.L., Miller, C.F., Walker, B.A., Wooden, J.L., Mazdab, F., Bea, F., 2006. Tracking magmatic processes through Zr/Hf ratios in rocks and Hf and Ti zoning in zircons: an example from the Spirit Mountain batholith, Nevada. Mineralogical Magazine 70, 517–543.

Compston, W., Williams, I.S., Meyer, C.E., 1984. U–Pb geochronology of zircons from lunar breccia 73217 using a sensitive high mass-resolution ion microprobe. Journal of Geophysical Research B 89 (Suppl.), 525–534.

Coogan, L.A., Hinton, R.W., 2006. Do the trace element compositions of detrital zircons require Hadean continental crust? Geology 34, 633–636.

Corfu, F., Hanchar, J.M., Hoskin, P.W.O., Kinny, P., 2003. Atlas of zircon textures. Reviews in Mineralogy and Geochemistry 53, 469–500.

Dana, E.S., 1916. A text-book of mineralogy; with an extended treatise on crystallography and physical mineralogy. J. Wiley & Sons, New York. 593 pp.

Deer, W.A., Howie, R.A., Zussman, H.J., 1978. Rock-forming minerals: orthosilicates, 1A: orthosilicates. Longman, London.

Dick, H.J.B., Meyer, P.S., Bloomer, S.H., Kirby, S.H., Stakes, D.S., Mawer, C.K., Von Herzen, R.P., Robinson, P.T., Adamson, A.C., Becker, K., Cannat, M., Emmermann, R.F.K., Gard, G., Goldberg, D., Hebert, R., Hertogen, J.G.H., Hoskins, H., Iturrino, G., Kassenaar, J.D.C., Kempton, P.D., Kikawa, E., Natland, J.H., Ozawa, K., Pariso, J., Scott, J.H., Swift, S.A., 1991a. Lithostratigraphic evolution of an in-situ section of oceanic layer 3. Proceedings of the Ocean Drilling Program, Scientific Results 118, 439–538.

Dick, H.J.B., Schouten, H., Meyer, P.S., Gallo, D.G., Bergh, H., Tyce, R., Patriat, P., Johnson, K.T.M., Snow, J., Fisher, A., 1991b. Tectonic evolution of the Atlantis II fracture zone. In: Von Herzen, R.P., Fox, J., Palmer-Julson, A., Robinson, P.R. (Eds.), Proceedings of the Ocean Drilling Program, Scientific Results 118. Ocean Drilling Program, College Station, TX, pp. 359–398.

Dick, H.J.B., Natland, J.H., Alt, J.C., Bach, W., Bideau, D., Gee, J.S., Haggas, S., Hertogen, J. G.H., Hirth, G., Holm, P.M., Ildefonse, B., Iturrino, G.J., John, B.E., Kelley, D.S., Kikawa, E., Kingdon, A., LeRoux, P.J., Maeda, J., Meyer, P.S., Miller, D.J., Naslund, H. R., Niu, Y.-L., Robinson, P.T., Snow, J., Stephen, R.A., Trimby, P.W., Worm, H.-U., Yoshinobu, A., 2000. A long in situ section of the lower ocean crust; results of ODP Leg 176 drilling at the Southwest Indian Ridge. Earth and Planetary Science Letters 179, 31–51.

Dick, H.J.B., Lin, J., Schouten, H., 2003. An ultraslow-spreading class of ocean ridge. Nature 426, 405–408.

Finch, R.J., Hanchar, J.M., 2003. Structure and chemistry of zircon and zircon-group minerals. Reviews in Mineralogy and Geochemistry 53, 1–25.

Finch, R.J., Hanchar, J.M., Hoskin, P.W.O., Burns, P.C., 2001. Rare-earth elements in synthetic zircon: part 2. A single-crystal X-ray study of xenotime substitution. American Mineralogist 86, 681–689.

Geisler, T., Pidgeon, R.T., Kurtz, R., van Bronswijk, W., Schleicher, H., 2003a. Experimental hydrothermal alteration of partially metamict zircon. American Mineralogist 88, 1496–1513.

Geisler, T., Rashwan, A.A., Rahn, M.K.W., Poller, U., Zwingmann, H., Pidgeon, R.T., Schleicher, H., Tomaschek, F., 2003b. Low-temperature hydrothermal alteration of natural metamict zircons from the Eastern Desert, Egypt. Mineralogical Magazine 67, 485–508.

Geisler, T., Schaltegger, U., Tomaschek, F., 2007. Re-equilibration of zircon in aqueous fluids and melts. Elements 3, 43–50.

Gillis, K.M., 1996. Rare earth element constraints on the origin of amphibole in gabbroic rocks from Site 894, Hess Deep. In: Mevel, C., Gillis, K.M., Allan, J.F., Meyer, P.S. (Eds.), Proceedings of the Ocean Drilling Program. Scientific results. Ocean Drilling Program, College Station, Texas, pp. 59–75.

Grimes, C.B., John, B.E., Kelemen, P.B., Mazdab, F., Wooden, J.L., Cheadle, M.J., Hanghoi, K., Schwartz, J.J., 2007. The trace element chemistry of zircons from oceanic crust: a method for distinguishing detrital zircon provenance. Geology 35, 643–646.

Grimes, C.B., John, B.E., Cheadle, M.J., Wooden, J.L., 2008. Evolution and timescales for accretion of slow-spreading oceanic crust: constraints from high resolution U–Pb zircon dating of a gabbroic crustal section at Atlantis Massif, 30° N, MAR. Geochemistry Geophysics Geosystems 9. doi:10.1029/2008GC002063.

Grimes, C.B., John, B.E., Cheadle, M.J., Mazdab, F.K., Wooden, J.L., Swapp, S., Schwartz, J.J., 2009. On the occurrence, trace element geochemistry, and crystallization history of zircon from in situ ocean lithosphere. Contributions to Mineralogy and Petrology 158, 757–783.

Hanchar, J.M., Finch, R.J., Hoskin, P.W.O., Watson, E.B., Cherniak, D.J., Mariano, A.N., 2001. Rare earth elements in synthetic zircon: Part 1. Synthesis, and rare earth element and phosphorus doping. American Mineralogist 86, 667–680.

Hart, S.R., Blusztajn, J., Dick, H.J.B., Meyer, P.S., Muehlenbachs, K., 1999. The fingerprint of seawater circulation in a 500-meter section of ocean crust gabbros. Geochimica et Cosmochimica Acta 63, 4059–4080.

Hinton, R.W., Upton, B.G.J., 1991. The chemistry of zircon; variations within and between large crystals from syenite and alkali basalt xenoliths. Geochimica et Cosmochimica Acta 55, 3287–3302.

Hosford, A., Tivey, M.A., Matsumoto, T., Dick, H.J.B., Schouten, H., Kinoshita, H., 2003. Crustal magnetization and accretion at the Southwest Indian Ridge near the Atlantis II fracture zone, 0–25 Ma. Journal of Geophysical Research 108. doi:10.1029/2001JB00064.

Hoskin, P., 2005. Trace element composition of hydrothermal zircon and the alteration of Hadean zircon from the Jack Hills, Australia. Geochimica et Cosmichimica Acta 69, 637–648.

Hoskin, P.W.O., Black, L.P., 2000. Metamorphic zircon formation by solid-state recrystallization of protolith igneous zircon. Journal of Metamorphic Geology 18, 423–439.

Hoskin, P.W.O., Schaltegger, U., 2003. The composition of zircon and igneous and metamorphic petrogenesis. Reviews in Mineralogy and Geochemistry 53, 27–62.

Hoskin, P., Kinny, P., Wyborn, D., 1998. Chemistry of hydrothermal zircon: investigating timing and nature of water–rock interaction. In: Arehart, G.B., Hulston, J.R., Balkema, A.A. (Eds.), Water rock Interaction. Totterdam, pp. 545–548.

Hoskin, P.W.O., Kinny, P.D., Wyborn, D., Chappell, B.W., 2000. Identifying accessory mineral saturation during differentiation in granitoid magmas; an integrated approach. Journal of Petrology 41, 1365–1396.

Ireland, T.R., Williams, I.S., 2001. Considerations in zircon geochronology by SIMS. Reviews in Mineralogy and Geochemistry 53, 215–241.

John, B.E., Foster, D.A., Murphy, J.M., Cheadle, M.J., Baines, A.G., Fanning, C.M., Copeland, P., 2004. Determining the cooling history of in situ lower oceanic crust-Atlantis Bank, SW Indian Ridge. Earth and Planetary Science Letters 222, 145–160.

Kamo, S.L., Krogh, T.E., Krogh, T.E., Kamo, S.L., Bohor, B.F., 1995. Chicxulub Crater source for shocked zircon crystals from the Cretaceous–Tertiary boundary layer, Saskatchewan; evidence from new U–Pb data fingerprinting the K/T impact site and determining the time of impact by U–Pb dating of single shocked zircons from distal ejecta. Geology 23, 281–284.

Krogh, T.E., Kamo, S.L., Bohor, B.F., 1993. Fingerprinting the K/T impact site and determining the time of impact by U–Pb dating of single shocked zircons from distal ejecta. Earth and Planetary Science Letters 119, 425–429.

Lee, J., Williams, I., Ellis, D., 1997. Pb, U and Th diffusion in natural zircon. Nature 390, 281–304.

Leroux, H., Reimold, W.U., Koeber, L.C., Hornemann, U., Doukhan, J.C., 1999. Experimental shock deformation in zircon: a transmission electron microscopic study. Earth and Planetary Science Letters 169, 291–301.

Liati, A., Froitzheim, N., Fanning, C.M., 2005. Jurassic ophiolites within the Valais Domain of the Western and Central Alps; geochronological evidence for re-rifting of oceanic crust. Contributions to Mineralogy and Petrology 149, 446–461.

Lissenberg, C.J., Rioux, M., Shimizu, N., Bowring, S.A., Mével, C., 2009. Zircon dating of oceanic crustal accretion. Science 323, 1017–1018.

Ludwig, K.R., 2001. SQUID 1.02. Berkeley Geochronology Center Spec. Pub. No. 2.

Ludwig, K.R., 2003. Isoplot 3.00: a geochronological toolkit for Microsoft Excel. Berkeley Geochronology Center Spec. Pub. No. 4.

Maas, R., Kinny, P.D., Williams, I.S., Froude, D.O., Compston, W., 1992. The Earth's oldest known crust; a geochronological and geochemical study of 3900–4200 Ma old detrital zircons from Mt. Narryer and Jack Hills, Western Australia. Geochimica et Cosmochimica Acta 56, 1281–1300.

MacLeod, C.J., Allerton, S., Dick, H.J.B., Robinson, P., Party, S.S., 1998. Geology of Atlantis Bank, SW Indian Ridge: preliminary results of RRS James Clark Ross Cruise 31. Eos, Transactions AGU 79, F893.

Mazdab, F.K., 2009. Characterization of flux-grown trace element-doped titanite using the high-mass-resolution ion microprobe (Shrimp-Rg). Canadian Mineralogist 47, 813–831.

Mazdab, F., Wooden, J.L., 2006. Trace element analysis in zircon by ion microprobe (SHRIMP-RG); technique and applications. Geochimica et Cosmochimica Acta 70, A405 (2006 Goldschmidt abstract volume).

McLelland, J.M., Bickford, M.E., Hill, B.M., Clechenko, C.C., Valley, J.W., Hamilton, M.A., 2004. Direct dating of Adirondack massif anorthosite by U–Pb SHRIMP analysis of igneous zircon: implications for AMCG complexes. GSA Bulletin 116, 1299–1317.

Meurer, W.P., Gee, J., 2002. Evidence for the protracted construction of slow-spread oceanic crust by small magmatic injections. Earth and Planetary Science Letters 201, 45–55.

Miranda, E.A., 2006. Structural Development of the Atlantis Bank Oceanic Detachment Fault System. Southwest Indian Ridge, University of Wyoming, Laramie. 457 pp.

Murakami, T., Chakoumakos, B.C., Ewing, R.C., Lumpkin, G.R., Weber, W.J., Lumpkin, G.R., 1991. Alpha-decay event damage in zircon rare-element mineralogy and internal evolution of the Rutherford #2 Pegmatite, Amelia County, Virginia; a classic locality revisited. American Mineralogist 76, 1510–1532.

Natland, J.H., Dick, H.J.B., 2001. Formation of the lower ocean crust and the crystallization of gabbroic cumulates at a very slowly spreading ridge. Journal of Volcanology and Geothermal Research 110, 191–233.

Natland, J.H., Dick, H.J.B., 2002. Stratigraphy and composition of gabbros drilled in Ocean Drilling Program Hole 735B, Southwest Indian Ridge; a synthesis of geochemical data. In: Natland, J.H., Dick, H.J.B., Miller, D.J., Von Herzen, R.P. (Eds.), Proceedings of the Ocean Drilling Program, Scientific Results (CD-Rom), p. 69.

Nemchin, A.A., Pidgeon, R.T., 1997. Evolution of the Darling Range Batholith, Yilgarn Craton, Western Australia; a SHRIMP zircon study. Journal of Petrology 38, 625–649.

O'Neil, J.R., Taylor, H.P., 1967. The oxygen isotope and cation exchange chemistry of feldspars. American Mineralogist 52, 1414–1437.

Pan, Y., 1997. Zircon- and monazite-forming metamorphic reactions at Manitouwadge, Ontario. The Canadian Mineralogist 35 (Part 1), 105–118.

Pidgeon, R.T., 1992. Recrystallisation of oscillatory zoned zircon; some geochronological and petrological implications. Contributions to Mineralogy and Petrology 110, 463–472.

Pidgeon, R.T., Nemchin, A.A., Hitchen, G.J., 1998. Internal structures of zircons from Archaean granites from the Darling Range Batholith; implications for zircon stability and the interpretation of zircon U–Pb ages. Contributions to Mineralogy and Petrology 132, 288–299.

Puga, E., Fanning, C.M., Nieto, J.M., Diaz de Federico, A., Pattison, D.R.M., St-Onge, M.R., Begin, N.J., 2005. Recrystallization textures in zircon generated by ocean floor and eclogite facies metamorphism; a cathodoluminescence and U/Pb SHRIMP study, with constraints from REE elements. The Canadian Mineralogist 43 (Part 1), 183–202.

Putnis, A., 2002. Mineral replacement reactions: from macroscopic observations to microscopic mechanisms. Mineralogical Magazine 66, 689–708.

Reddy, S.M., Timms, N.E., Trimby, P., Kinny, P.D., Buchan, C., Blake, K., 2006. Crystal–plastic deformation of zircon: a defect in the assumption of chemical robustness. Geology 34, 257–260.

Reddy, S.M., Timms, N.E., Pantleon, W., Trimby, P., 2007. Quantitative characterization of plastic deformation of zircon and geological implications. Contributions to Mineralogy and Petrology 153, 625–645.

Reddy, S.M., Timms, N.E., Hamilton, P.J., Smyth, H.R., 2009. Deformation-related microstructures in magmatic zircon and implications for diffusion. Contributions to Mineralogy and Petrology 157, 231–244.

Robinson, P.T., Dick, H.J.B., Natland, J.H., Alt, J.C., Bach, W., Bideau, D., Gee, J.S., Haggis, S., Hertogen, J., Hirth, G., Holm, P.M., Ildefonse, B., Iturrino, G.J., John, B.E., Kelley, D.S., Kikawa, E., Kingdon, A., LeRoux, P.J., Maeda, J., Meyer, P.S., Miller, D.J., Naslund, H.R., Niu, Y.L., Snow, J., Stephen, R.A., Trimby, P.W., Worm, H.U., Yoshinobu, A., 2000. Lower oceanic crust formed at an ultra-slow-spreading ridge; Ocean Drilling Program Hole 735B, Southwest Indian Ridge. Special Paper - Geological Society of America 349, 75–86.

Rubatto, D., Hermann, J., 2003. Zircon formation during fluid circulation in eclogites (Monviso, Western Alps); implications for Zr and Hf budget in subduction zones. Geochimica et Cosmochimica Acta 67, 2173–2187.

Sambridge, M.S., Compston, W., 1994. Mixture modeling of multi-component data sets with application to ion-probe zircon ages. Earth and Planetary Science Letters 128, 373–390.

Schaltegger, U., Fanning, C.M., Guenther, D., Maurin, J.C., Schulmann, K., Gebauer, D., 1999. Growth, annealing and recrystallization of zircon and preservation of monazite in high-grade metamorphism; conventional and in-situ U–Pb isotope, cathodoluminescence and microchemical evidence. Contributions to Mineralogy and Petrology 134, 186–201.

Schärer, U., 1984. The effect of initial ^{230}Th disequilibrium on young U–Pb ages: the Makalu case, Himalaya. Earth and Planetary Science Letters 67, 191–204.

Schwartz, J.J., John, B.E., Cheadle, M.J., Miranda, E.A., Grimes, C.B., Wooden, J.L., Dick, H.J.B., 2005. Dating the growth of oceanic crust at a slow-spreading ridge. Science 310, 654–657.

Schwartz, J.J., John, B., Cheadle, M.J., Reiners, P.W., Baines, A.G., 2009. Cooling history of Atlantis Bank oceanic core complex: evidence for hydrothermal activity 2.6 Ma off axis. Geochemistry Geophysics Geosystems 10. doi:10.1029/2009GC002466.

Spandler, C., Hermann, J., Rubatto, D., 2004. Exsolution of thortveitite, yttrialite, and xenotime during low-temperature recrystallization of zircon from New Caledonia, and their significance for trace element incorporation in zircon. American Mineralogist 89, 1795–1806.

Speer, J.A., 1980a. The actinide orthosilicates. Reviews in Mineralogy and Geochemistry 5, 113–135.

Speer, J.A., 1980b. Zircon. Reviews in Mineralogy and Geochemistry 5, 67–112.

Stacey, J.S., Kramers, J.D., 1975. Approximation of terrestrial lead isotope evolution by a two-stage model. Earth and Planetary Science Letters 26, 207–221.

Tera, F., Wasserburg, G.J., 1972. U–Th–Pb systematics in three Apollo 14 basalts and the problem of initial Pb in lunar rocks. Earth and Planetary Science Letters 14, 281–304.

Timms, N.E., Kinny, P., Reddy, S.M., 2006. Enhanced diffusion of uranium and thorium linked to crystal plasticity in zircon. Geochemical Transactions 7. doi:10.1186/1467-4866-7-10.

Tomaschek, F., Kennedy, A.K., Villa, I.M., Lagos, M., Ballhaus, C., 2003. Zircons from Syros, Cyclades, Greece; recrystallization and mobilization of zircon during high-pressure metamorphism. Journal of Petrology 44, 1977–2002.

Watson, E.B., Harrison, T.M., 2005. Zircon thermometer reveals minimum melting conditions on earliest earth. Science 308, 841–844.

Whitehouse, M.J., Kamber, B.S., 2002. On the overabundance of light rare earth elements in terrestrial zircon and its implications for Earth's earliest magmatic differentiation. Earth and Planetary Science Letters 204, 333–346.

Williams, I.S., 1998. U–Th–Pb geochronology by ion microprobe. In: McKibben (Ed.), Applications of microanalytical techniques to understanding mineralization processes: Soc. Econ. Geol. , pp. 1–35.

Wooden, J.L., Mazdab, F.K., Barth, A.P., Miller, C.F., Lowery, L.E., 2006. Temperatures (Ti) and compositional characteristics of zircon: early observations using high mass resolution on the USGS-Stanford SHRIMP-RG. Geochimica et Cosmichimica Acta 70, A707 (2006 Goldschmidt abstract volume).